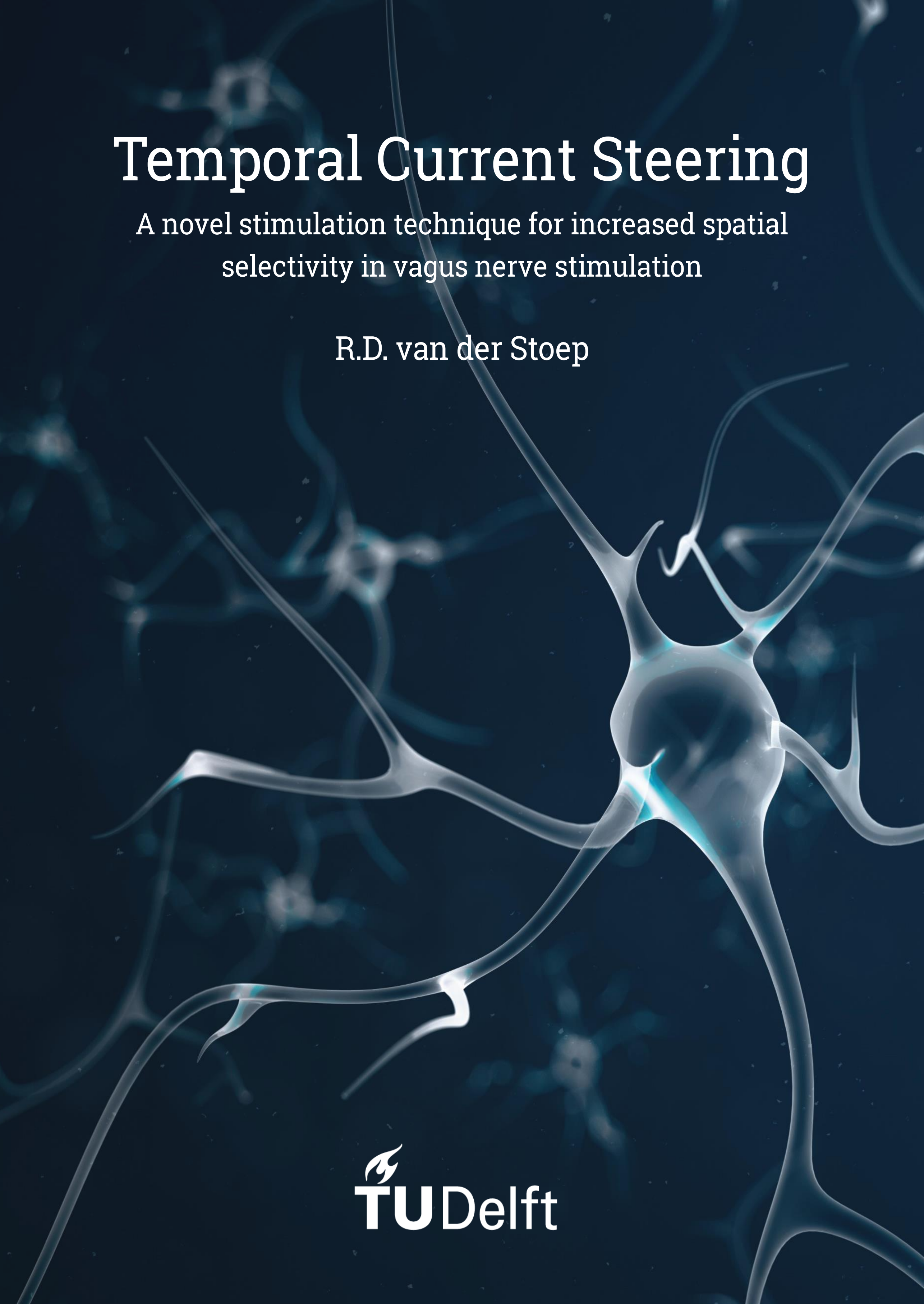

Temporal Current Steering

A novel stimulation technique for increased spatial selectivity in vagus nerve stimulation

R.D. van der Stoep

TU Delft

TEMPORAL CURRENT STEERING

A NOVEL STIMULATION TECHNIQUE FOR INCREASED SPATIAL SELECTIVITY IN VAGUS NERVE STIMULATION

by

Remco Dingeman VAN DER STOEP

to obtain the degree of Master of Science
at the Delft University of Technology
to be defended publicly on Monday July 8, 2024 at 14:00

Student number:	4612361	
Project duration:	April, 2023 – July, 2024	
Thesis committee:	Prof. dr. ir. W.A. Serdijn,	TU Delft, supervisor
	Ir. F. Varkevisser,	TU Delft, daily supervisor
	Dr. V. Giagka,	TU Delft

CONTENTS

Summary vii

Acknowledgements ix

1. Introduction 1
- 1.1. Background . . . 1
  - 1.1.1. Anatomy of the Vagus Nerve . . . 1
  - 1.1.2. Electrical Neuromodulation . . . 2
- 1.2. Problem Statement and Research Question . . . 7
- 1.3. Chapter Organization . . . 7

2. Literature Review 9
- 2.1. Non-Invasive Neurostimulation Techniques . . . 9
  - 2.1.1. Transcutaneous Electrical Nerve Stimulation . . . 9
  - 2.1.2. Temporal Interference . . . 10
  - 2.1.3. Nano-Second Electric Pulse Stimulation . . . 13
  - 2.1.4. Transcranial Electric Stimulation . . . 17
  - 2.1.5. Transcranial Magnetic Stimulation . . . 18
- 2.2. State of the art . . . 18
  - 2.2.1. Invasive Devices . . . 19
  - 2.2.2. Non-Invasive Devices . . . 19
  - 2.2.3. Advancements in Stimulation Selectivity . . . 20
- 2.3. Literature Discussion . . . 23
- 2.4. Thesis Objective and Approach . . . 24

3. Methods 25
- 3.1. Simulation Environment . . . 25
  - 3.1.1. Neuron . . . 25
  - 3.1.2. Python . . . 27
- 3.2. Implementation of Optimization Algorithms . . . 30
  - 3.2.1. Genetic Algorithm . . . 30
  - 3.2.2. Particle Swarm Optimization . . . 32
- 3.3. Simulation Parameters and Optimization . . . 34

4. Results 37
- 4.1. Model Validation . . . 37
- 4.2. Genetic Algorithm vs Particle Swarm Optimization . . . 38
- 4.3. Results Multistart . . . 39
  - 4.3.1. Trendline Fitness . . . 40

4.3.2. Best result 41
4.3.3. Waveform Identification 44
4.4. Temporal Current Steering vs Direct Current Steering 46

5. Discussion and Conclusion **51**
5.1. Discussion 51
5.1.1. Recommendations for Future Work 52
5.2. Conclusion 53

Bibliography **55**

A. Additional Figures **67**

SUMMARY

Cervical Vagus Nerve Stimulation (CVNS) has shown efficacy in treating depression, therapy-resistant epilepsy, and is being explored for conditions such as obesity and migraine [1–3]. The side effects of whole nerve stimulation, which is currently the only approved method, can be minimized using spatially selective stimulation [4–7]. This thesis introduces Temporal Current Steering (TCS), a novel stimulation technique aimed at enhancing spatial selectivity for CVNS. TCS introduces a temporal variation to standard current steering, creating an electric field that varies both temporally and spatially. With this study, enhanced spatial selectivity was confirmed through simulations of extracellular stimulation of neurons with time-dependent waveforms on two electrodes located on a single plane. Particle swarm optimization was employed over 2000 iterations and 98 runs to identify a waveform with the highest spatial selectivity. The optimal solution achieved a 30% improvement over a single electrode placed directly in line with the target and a 31% improvement over the standard direct current steering technique, simulated in the same model. The findings of this thesis suggest that TCS can increase spatial selectivity in invasive stimulation, although further simulations are needed for non-invasive applications with greater electrode-to-neuron distances.

Acknowledgements

To complete my thesis and thereby finish the master's program in Biomedical Engineering, I reflect happily on the decision to embark on this adventure. The outcome is a thesis and a project of which I am proud, and that I could not have accomplished alone. Firstly, I would like to express my gratitude to Wouter for providing me with the opportunity to work on this project and for the autonomy I was given. I am also thankful for his guidance and support throughout, together with Francesc. Special thanks go to Francesc for always being available for questions and feedback. Thank you to Dr. Giagka for taking the time to read this thesis and participate in my thesis committee. The Bioelectronics group makes a lot of efforts to ensure that you are not just a student, but a member of the team, for which I am grateful.

I would like to thank Maikey for being an always available sparring partner, and Margherita for her support and motivation to constantly strive for more. However, the most special thanks go to my family, who unquestionably supported me throughout my entire student life. They never asked for anything in return and trusted my decisions. Thank you.

Remco van der Stoep
Barendrecht, June 2024

1

INTRODUCTION

Approximately 30% of all epilepsy patients are drug-resistant; for these patients, cervical vagus nerve stimulation (CVNS) can be an alternative treatment [8]. Besides treating epilepsy, CVNS has also proven to be a viable option for treating depression, and its applications for conditions such as obesity, migraines, and cardiovascular disease are being explored [1–3, 9]. For current stimulating devices, both invasive and non-invasive, the primary side effects result from stimulating the entire vagus nerve (VN) [4–7]. Therefore, increasing spatial selectivity is desired to reduce side effects caused by the unwanted activation of fibers within the VN [4, 5, 10, 11]. In this thesis, a novel method of stimulating the cervical vagus nerve with spatial selectivity is introduced, offering enhanced spatial selectivity for CVNS.

1.1. BACKGROUND

In this paragraph, background information is given about the anatomy of the vagus nerve and the process of electrically stimulating neurons to better understand the process of stimulation the cervical vagus nerve.

1.1.1. ANATOMY OF THE VAGUS NERVE

There are two vagus nerves located in the body, originating from the medulla and extending down to the abdomen. These nerves collectively account for 90% of all parasympathetic fibers in the body, reaching virtually every organ in the thoracic and abdominal cavities. The fibers composing the vagus nerve are ganglionic axons that typically synapse in terminal ganglia located within the walls of the target organs [12].

Each axon is part of a neuron, which consists of three main parts: the cell body or soma, the axon, and the dendrites. The dendrites serve as the primary receptive or input regions, providing a surface area for receiving signals. The cell body is the major biosynthetic (involved in the production of chemical compounds) and metabolic center of a neuron. The axon is responsible for generating and conducting nerve impulses or action potentials (AP) [12].

Within the vagus nerve the fibers can be classified into A, B and C groups based on their properties [13, 14]. The A fibers have the largest diameter and the lowest activation threshold, then the B fibers and then the C fibers with the highest threshold. About 20% of all fibers consist of type A and B combined, and approximately 80% are type C [13]. The latest research indicates that the fibers are spatially organized per function or somatotopically [4, 15].

In the neck, the vagus nerve is referred to as the cervical vagus nerve (CVN) and is located relatively superficial to the skin with minimal intervening structures. This anatomical feature has been utilized for the placement of implantable stimulation devices [2]. Additionally, it could be advantageous for non-invasive stimulation techniques, as the electric field does not need to penetrate deeply.

The distance from the skin on the neck to the CVN is 36mm according to Shin et al. and Hammer et al. [16][17]. However, stimulation devices already using non-invasive CVN stimulation report a distance of 12.5mm [7]. This discrepancy could come because of pressing the stimulation device against the skin shortening the distance, or a difference in angle since Shin et al. measures orthogonal to the midline, see Figure 1.1.

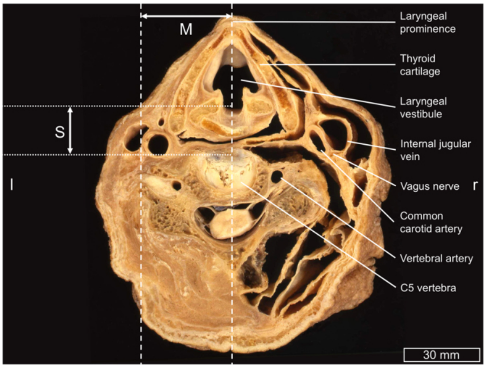

Figure 1.1.: The paraffin-embedded axial-plane section corresponding to the C5 vertebral body. M represents the midline distance, which is the lateral distance between the laryngeal prominence and the cervical vagus nerve. S denotes the skin distance, which is the anterior-posterior distance between the skin surface and the cervical vagus nerve in the sagittal direction. [17]

Table 1.1 shows properties of the CVN that could be relevant for future simulations like the CVN diameter and number of fascicles.

1.1.2. ELECTRICAL NEUROMODULATION

A neuron transmits an impulse using two mechanisms: electrical conduction along the neuron itself due to ion channels, and chemical conduction between neurons at the synapse. The neuron exhibits a potential difference across its cell membrane

Table 1.1.: Description and values of cervical vagus nerve morphometrics [17]

Parameter	Mean ± standard deviation
Cross-sectional area	$7.2 \pm 3.1\,\mathrm{mm}^2$
Greater diameter	$5.1 \pm 1.5\,\mathrm{mm}$
Lesser diameter	$4.1 \pm 1.3\,\mathrm{mm}$
Midline distance	$34.5 \pm 6.2\,\mathrm{mm}$
Skin distance	$36.2 \pm 9.4\,\mathrm{mm}$
Nerve fascicle number	5.2 ± 3.5

due to variations in ion concentrations inside and outside the cell. This difference in ions creates an inner surface potential Φ_i and outer surface potential Φ_o, with the membrane acting as a barrier. The membrane voltage V_m is calculated by subtracting Φ_o from Φ_i [18], as shown in (1.1). If the membrane voltage exceeds a threshold potential an AP is created.

$$V_m = \Phi_i - \Phi_o \tag{1.1}$$

Through electrical neuromodulation, Φ_o can be altered by subjecting it to an electric field (E-field). The applied E-field increases the membrane voltage, triggering voltage-gated ion channels in the membrane. Once the threshold voltage is reached, rapid changes in ion concentrations inside the axon generate an AP. The resulting AP follows a characteristic waveform regardless of the stimulus strength or duration. Ion pumps in the membrane work to restore the membrane voltage to its resting value [18], as illustrated in Figure 1.2.

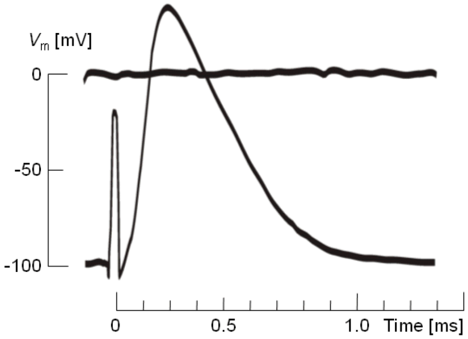

Figure 1.2.: A nerve impulse recorded from a cat after a transthreshold stimulus. The stimulus artifact is visible at t = 0. [18]

The AP generates a potential difference between the excited and unexcited regions, leading to the generation of local circuit currents. These currents flow toward the unexcited regions, triggering new APs and allowing the impulse to propagate along the axon without attenuation. In myelinated axons, APs can only occur at the nodes of Ranvier, where the myelin sheath is interrupted. This mode of propagation increases the speed of impulse conduction, as depicted in Figure 1.3 [18].

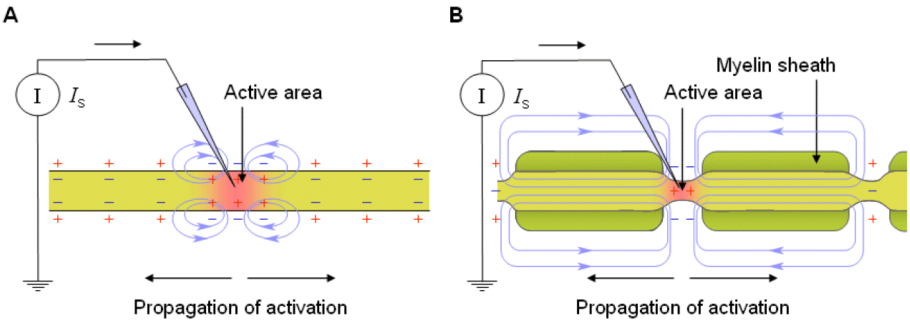

Figure 1.3.: Travel of AP at an unmyelinated axon (A) and myelinated axon (B). [18]

As mentioned, if and when an AP is created, is dependent on reaching the threshold potential. Which on its own is dependent on the membrane current which changes the ion concentrations and therefore the membrane voltage. In 1952 Hodgkin and Huxley developed a model for the currents involved in producing an AP from a giant squid axon which is still relevant. The model describes the total membrane current (I_m) as the sum of four components (1.2) [19].

$$I_m = I_{Na} + I_K + I_l + I_c \tag{1.2}$$

Where:

I_m is the membrane current
I_c is the capacitive current
I_{Na} is the Sodium ion current
I_K is the Potassium current
I_l is the leakage current

Of particular interest for the activation function are the sodium and potassium currents. Hodgkin and Huxley proposed that electrically charged particles present in ion gates determine whether the gates are open or closed. These particles can exist in two states: open or closed.

For the potassium current (similar principles apply to sodium), the movement of particles (n) is governed by voltage-dependent functions represented by α and β, as depicted in (1.3) and (1.4). Making the membrane voltage less negative increases the value of α, opening more ion gates. This process allows the membrane voltage to become more less negative, increasing α exponentially, thereby increasing n and consequently the potassium conductance (G_K) (1.5) and membrane voltage. This cycle continues until the threshold voltage is reached, where α exceeds β, initiating the action potential as depicted in Figure 1.4, where α and β cross each other.

If stimulation ceases before this point, β remains larger than α, causing ion gates to close and the membrane voltage to return to resting potential as the axon seeks equilibrium.

$$0 \leq n \leq 1 \tag{1.3}$$

$$n \underset{\beta_n}{\overset{\alpha_n}{\leftrightarrows}} (1 - n) \tag{1.4}$$

$$G_K = G_{K,max} * n^4 \tag{1.5}$$

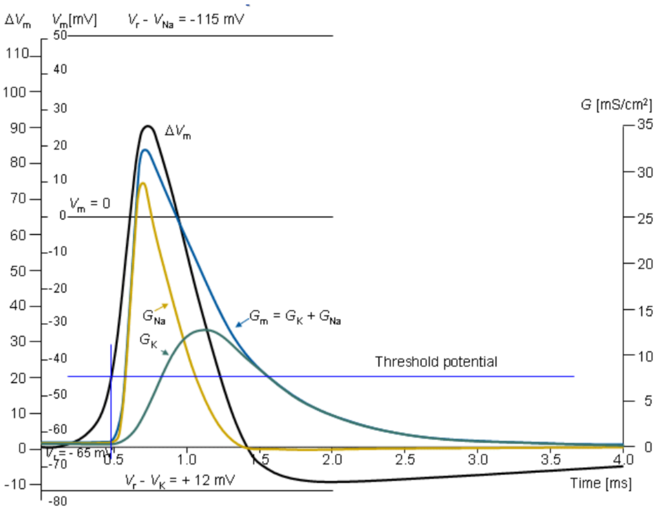

Figure 1.4.: Sodium (G_{Na}) and Potassium (G_k) conductances and their sum (G_m). Once the membrane voltage (ΔV_m) exceeds the threshold potential, an action potential is generated. [18]

The stimulation of V_m generates a membrane current that, depending on its strength, takes a certain time to create an action potential due to the physical process of opening ion gates. This relationship between current strength and stimulation time is described by the strength-duration (SD) curve [18]. The SD curve illustrates the minimum induced membrane current required to reach the threshold potential for a given pulse duration t, known as the threshold current (I_t). Understanding the relationship $Q = \int I dt$, it is possible to plot the threshold charge (Q_t) against pulse duration, as shown in Figure 1.5B. The rheobase current (I_0) represents the lowest intensity current capable of generating an action potential; any current below this threshold will fail to induce an action potential regardless of pulse duration. Similarly, the rheobase charge (Q_0) denotes the minimum charge required for action potential generation. For short pulse durations, achieving this minimum charge necessitates high current intensities, leading to the rapid increase in threshold current observed in Figure 1.5A [20].

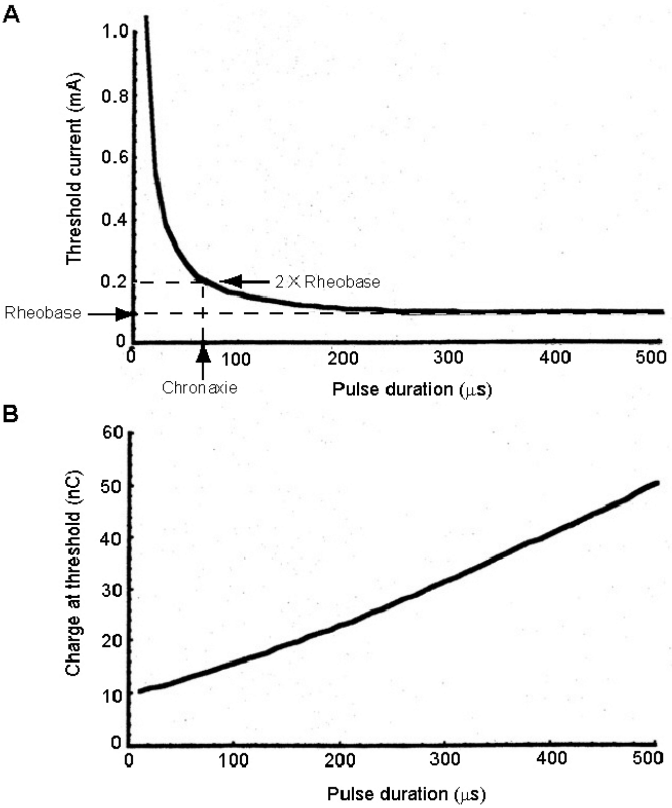

Figure 1.5.: Strenght duration curve plotting threshold current vs. pulse duration (A) and charge threshold vs pulse duration (B) [21]

By simulating or conducting experiments, multiple threshold currents can be determined for specific pulse durations. These data points can then be used to fit the SD curve illustrating the relationship between stimulation parameters and action potential initiation [22]. Understanding how these potential differences, currents, and pulse durations influence action potential generation provides valuable insights into the mechanisms underlying various stimulation techniques.

1.2. PROBLEM STATEMENT AND RESEARCH QUESTION

Currently, the only non-invasive method for CVNS is the GammaCore, which achieves selectivity by stimulating all fibers above a certain threshold. This means that bodily functions controlled by fibers with a lower threshold cannot be selectively stimulated without causing side effects. Spatially selective stimulation of the CVN offers a solution, as evidence suggests that the fibers in the vagus nerve are spatially organized by function [14]. Creating this selectivity is challenging for non-invasive devices due to the nerve's distance from the skin surface and the attenuation of the E-field. For invasive devices, selectivity is being explored through current steering, which could reduce side effects and expand use cases by enhancing spatial selectivity [5, 11]. In other fields, such as deep brain stimulation, non-invasive stimulation techniques are explored that use specific waveforms to increase spatial selectivity [23, 24]. Given this context, the main objective of this thesis is defined as follows:

Exploring non-invasive stimulation techniques to enhance spatial selectivity for cervical vagus nerve stimulation.

1.3. CHAPTER ORGANIZATION

This thesis will be outlined as follows: First, in chapter 2, a literature review is presented, providing current non-invasive stimulation techniques and state-of-the-art CVNS techniques. At the end of chapter 2, a novel method for spatially selective stimulation will be presented. The methods to validate this technique by means of simulation are discussed in chapter 3. The results of the simulation and comparison to direct current steering are presented in chapter 4. Finally, the results are discussed, and future recommendations are given in chapter 5, after which the conclusion is presented in section 5.2.

2

LITERATURE REVIEW

The proximity of the CVN to the skin surface offers some advantages in avoiding unintended fiber activation during non-invasive stimulation, as there are no intervening nerves responsible for critical body functions in that area [17]. However, this advantage comes at the cost of lower spatial selectivity compared to invasive methods, due to the wider distribution of the E-field in the surrounding space. An additional complexity is that stimulation can only occur from one plane, the surface of the neck. While spatial selectivity is being explored for invasive stimulation, methods from other fields that aim to increase spatial selectivity with non-invasive stimulation might provide a different approach.

This literature review aims to assess existing non-invasive electrical neurostimulation techniques to identify a method that achieves greater spatial selectivity for CVNS than currently available.

2.1. NON-INVASIVE NEUROSTIMULATION TECHNIQUES

This section provides an overview of some non-invasive stimulation techniques used for stimulating neurons. This is aimed at gaining a better understanding of non-invasive stimulation and exploring potential new techniques for CVNS.

2.1.1. TRANSCUTANEOUS ELECTRICAL NERVE STIMULATION

Transcutaneous Electrical Nerve Stimulation (TENS) is a technique that uses electrodes placed on the skin surface to control pain or stimulate motor nerves [25–30]. Electrical current is applied through at least one pair of electrodes, generating a potential gradient that depolarizes excitable tissue beneath the electrodes. When the potential exceeds a certain threshold, the excitable tissue is activated [26, 28]. The clinical effectiveness of TENS is controversial, and the exact mechanisms by which it reduces pain are not fully understood. The technique employs direct current or various frequencies, categorized as high frequency, low frequency, or burst [27, 29]. The intensity of the signal is regulated by increasing the current until the patient feels a comfortable tingling sensation. The most common theory is that TENS affects neurons in a way that inhibits their firing [27, 29, 31].

Stimulation is primarily limited by patient discomfort, making the activation of deeper neurons challenging since higher amplitudes, which induce more pain, are required [25, 26, 32]. This issue also applies to electrode size; smaller electrodes provide higher selectivity but also greater current density, leading to increased pain [26]. Several studies have aimed to find optimal electrode designs or placements that achieve the highest selectivity with the lowest current density [25, 33]. Electrode arrays have been proposed to dynamically adjust the size and position of the active region of a stimulating electrode, thereby reducing the time-consuming process of finding the optimal electrode position and size, and allowing for repositioning of the stimulated area without physically changing the electrode positions [26, 34, 35]. A downside of electrode arrays is that axons can lie between two electrodes, requiring more current from both electrodes to achieve the same effect as a single electrode directly above the axon [33].

Additionally, higher frequencies than normal have been tested to determine if they can stimulate axons in deeper tissue [36]. The model revealed that high-frequency signals generated larger potentials at depth compared to low frequencies, but this did not result in lower stimulation thresholds. This was hypothesized to be because the membrane is less susceptible to high frequencies. Moreover, while deeper nerves were activated, so were other nerves in its path [36].

It is desirable to find methods to generate activation using TENS in deeper tissues without greatly increasing patient comfort [32]. The success rate with TENS could be improved by careful attention to electrode placement, stimulation parameters, and patient education [31].

One of the benefits of TENS is that patients can self-administer the treatment and is therefore also a common treatment method [27]. However, the wide range of stimulation parameters used makes it difficult to draw definitive conclusions about TENS. Different studies report applied currents ranging from single milliamperes to tens of milliamperes [29, 30, 35]. There is consensus that deep stimulation is limited by the amplitude that the patient can tolerate, and a multiple-electrode design would be beneficial to reduce the effort in finding the optimal stimulation site.

2.1.2. TEMPORAL INTERFERENCE

Temporal interference (TI) uses a combination of techniques to stimulate a particular point inside tissue. Two electrode pairs are placed on the skin surface, each producing a high-frequency E-field inside the tissue. Applying this to the brain, Grossman et al. hypothesized that, because the neurons behave like a low-pass filter, if the stimulation frequency is high enough no stimulation occurs [23], see Figure 2.1A, location II. Using this characteristic each of the electrode pairs individually does not stimulate a neuron. Now the electrode pairs are placed in such a way that in a small area of the brain, the two electric fields interfere with each other, and following superposition the frequency of the electric field here becomes $(f_1 + f_2)/2$, see Figure 2.1A, location I. If $f_2 = f_1 + \Delta f$ where Δf is a low frequency, the envelope at location I will follow this low frequency. Following Grossman et al. theory the neurons will follow this low-frequency envelope and cause a stimulation [23] see Figure 2.1B, graph I. By altering the location of the electrodes and the stimulation frequencies, different locations in the brain can be stimulated without stimulating other parts because here one of the two electric fields is not strong enough to create the low-frequency envelope needed for stimulation, see Figure 2.1B, graph II.

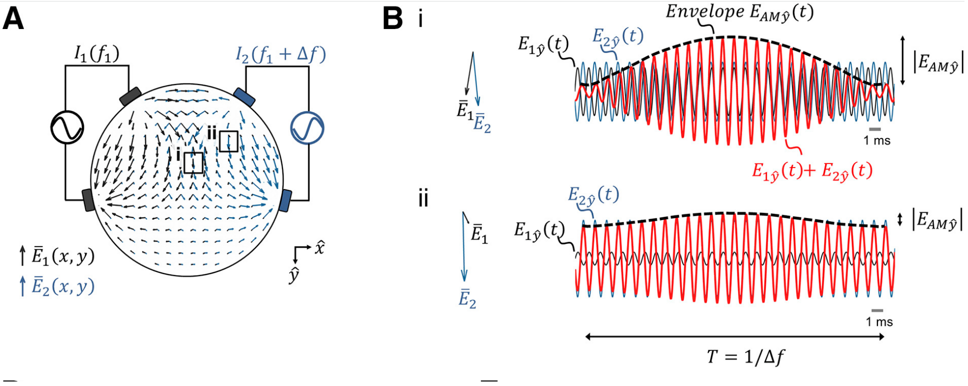

Figure 2.1.: (A) Two electrode pairs generate each an E-field inside the brain. (B) At location I superposition of the two fields generate an envelope with a frequency low enough for the neurons to follow. At other locations like II one of the two E-fields is not strong enough.[23]

Modeling showed that by changing electrode configuration and current sources it was possible to alter the location where the superposition of the two E-fields creates a strong enough envelope to cause neuron stimulation [23]. Testing this theory in living mice resulted in the stimulation of neurons when an envelope of 10 Hz was present and no stimulation when no TI was present [23].

Grossman et al.'s theory relies on the primary assumption that neurons do not elicit a response to high-frequency stimulation, and consequently, that neuron activation only occurs where the electric field is modulated to a lower frequency. However, this assumption is contradicted by the findings of Mirzakhalili et al. and Budde et al.

Firstly, there are no actual low frequencies present in the signals used for TI, as depicted in Figure 2.2B. Since genuine low frequencies are lacking, a mere low-pass filter is inadequate for extracting an envelope from the stimulus. Mirzakhalili et al. proposed that nonlinearities in ion channels result in signal rectification, enabling the extraction of a low frequency, as illustrated in Figure 2.2C. To validate this hypothesis, they conducted simulations after removing ion channels, observing an inability of neurons to extract the envelope, as shown in Figure 2.2D [37]. Thus, while the membrane response to TI can not simply be attributable to a low-pass filter, it can effectively extract the envelope when considering the entire model, inclusive of ion currents, as depicted in Figure 2.2E and Figure 2.2F.

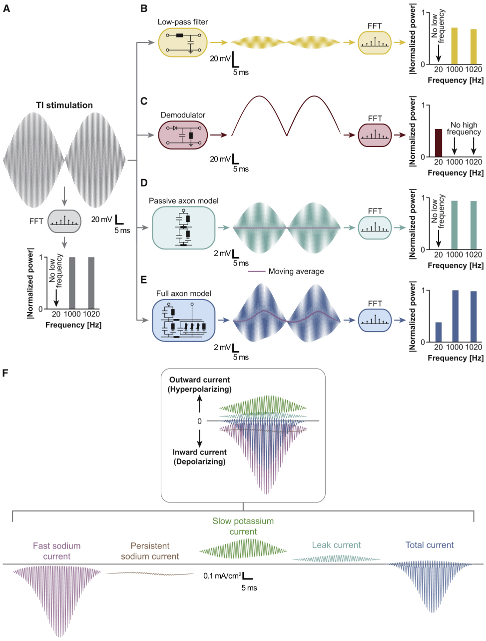

Figure 2.2.: Output waveforms created by putting a temporal wave (A) through different membrane dynamic models. (B) Low-pass filter (C) Demodulator (D) Passive axon model (no ion channels) (E) Active axon model with ion channels (F) The total neuron current split up into individual components. [37]

Secondly, both Mirzakhalili et al. and Budde et al. have illustrated that neurons outside the targeted area respond to the applied high-frequency stimulation through either conduction blocking (inhibition of action potential propagation) or tonic firing (sustained firing) [37][38]. Figure 2.3 presents the firing of axons over time at locations up to ± 4 mm from the target site. As depicted in Figure 2.3A, TI indeed elicits periodic firing around the target location (0 mm), whereas in the absence of TI, as shown in Figure 2.3B, such periodic firing is absent. Further away from the target location, both TI and No-TI induce conduction blocking as well as tonic firing, indicating that the high frequency E-field does affect neurons [37]. In Figure 2.4, Budde et al. demonstrate, using a cuff electrode on a rat's sciatic nerve, that mere envelope extraction cannot fully account for neuron activation. With only a 2000 Hz signal present, tonic firing is observed. Introducing the 2020 Hz signal gradually appears to modulate the stimulus above and below the threshold due to the summation of the two signals, suggesting the neuron's integrating capability rather than mere envelope extraction [38].

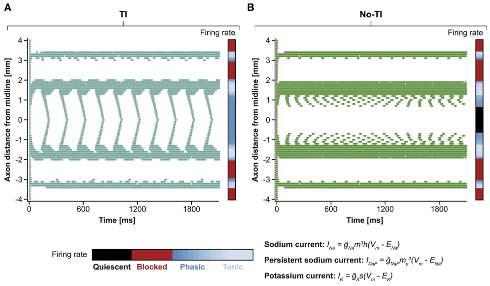

Figure 2.3.: (A) Neural response to temporal interference at different locations. (B) Neural response to only high-frequency signals at different locations. At an axon distance of zero, it can be seen that temporal interference (A) induces firing consistent with the envelope frequency, whereas with no temporal interference (B), this is not the case. Moving away from an axon distance equal to zero, both temporal interference and no temporal interference look alike and cause blocking and firing at the same distances. [37]

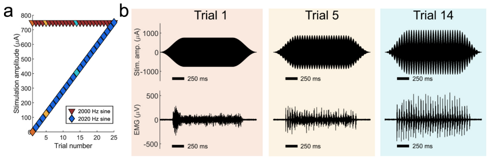

Figure 2.4.: The introduction of the 2020Hz signal to the original 2000Hz signal (A) seems to show an integrating capability of the neuron as highlighted by trial 1, 5 and 15 (B)[38]

In conclusion, TI not only stimulates the intended target region but also induces effects elsewhere due to the presence of high-frequency E-fields. These high frequencies can lead to tonic firing or conduction blocking in areas where the high-frequency E-field is active. Nevertheless, it is feasible to stimulate a specific region with periodic firing using TI. This capability may prove advantageous in certain applications where conduction blocking or tonic firing of surrounding neurons is not a concern or is even desirable.

2.1.3. NANO-SECOND ELECTRIC PULSE STIMULATION

The concept of electroporation has been established since the 1970s [39]. It involves the use of high E-fields to permeabilize a cell membrane, facilitating the uptake of molecules. Electroporation occurs when the transmembrane potential superimposed on the resting transmembrane potential exceeds a threshold value [40]. While this threshold value has been estimated to be around 1V [41], later studies found it to be approximately 200 mV [42]. Despite these variations, both values are higher than the threshold required to induce an action potential. To achieve these thresholds, according to (2.1) [40], the applied electric field needs to be in the order of MV/m since the cell radius is in the order of μm. Given that intracellular structures are even smaller than the cell itself, it is evident that these structures will not be permeabilized by electric fields capable of permeabilizing the outer cell membrane [40].

$$\Delta V_m = f E_{ext} r \cos(\Phi) \tag{2.1}$$

Where:

f is a factor depending on shape
ΔV_m is the trans-membrane potential
E_{ext} is the applied E-field
r is the cell radius
Φ is the angle with respect to E_{ext}

The time required to charge the transmembrane potential is dependent on the charging time constant, which considers the electrical parameters of both the cell and the medium it is in, and is approximately 75 ns [43]. Schoenbach et al. proposed that by combining pulse duration, electric field strength, cell size, and medium properties, it is possible to induce electroporation of intracellular membranes [43]. To achieve this effect, the pulse duration needs to be shorter than the charging time of the outer membrane, while the electric fields need to be high enough to induce permeabilization of the smaller intracellular membranes [39]. This results in high-intensity electric field pulses in the range of nanoseconds.

Pakhomov et al. introduced another aspect to nanosecond stimulation, known as nanosecond electric pulses (nsEP), employing a bipolar pulse configuration. One effect of nsEP they describe is the generation of nanopores that allow ion conduction [24]. This is interesting because with sufficient ion mobilization, an AP can be generated. However, simply applying nsEP affects all encountered tissue and may also induce other effects such as apoptosis [44]. Pakhomov et al. hypothesized that changing the unipolar pulse to a bipolar pulse it would mitigate the effect of a unipolar pulse. The addition of a pulse of opposite polarity cancels out the effect of the first pulse, thereby limiting this undesired impact [24].

Despite this cancellation reducing effects, the primary challenge with nsEP remains understanding its impact on cell damage through permeabilization and its precise mechanism for inducing an AP. Encouragingly, Casciola et al. reported that a 12-ns stimuli at 4.1-11 kV could generate an AP by activating voltage-gated sodium channels without involving permeabilization as an intermediate step [45]. This finding gains further support from simulations demonstrating AP induction using nsEP with pulses of only a few millivolts, well below the levels required for electroporation [46].

In theory, nsEP can stimulate without inducing electroporation, and using bipolar pulses allows cancellation of the effect in non-targeted areas. Combining these characteristics, Gianulis et al. devised the cancellation of bipolar cancellation (CANCAN-ES) technique. With CANCAN-ES, two electrodes emit a bipolar nsEP which should produce no effect. At the target site, superposition of both signals then cancels out the bipolar effect and induces an AP, as shown in Figure 2.5 [47].

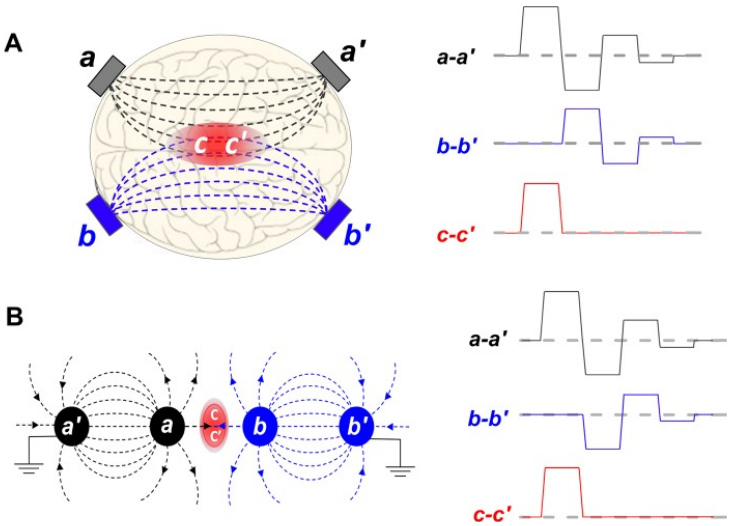

Figure 2.5.: CANCAN-ES technique [47]

In practice these two bipolar waves do not cancel each other perfectly everywhere except for where you want them to meet, so there are incomplete compensations at other locations resulting in various complex waveforms see Figure 2.6.

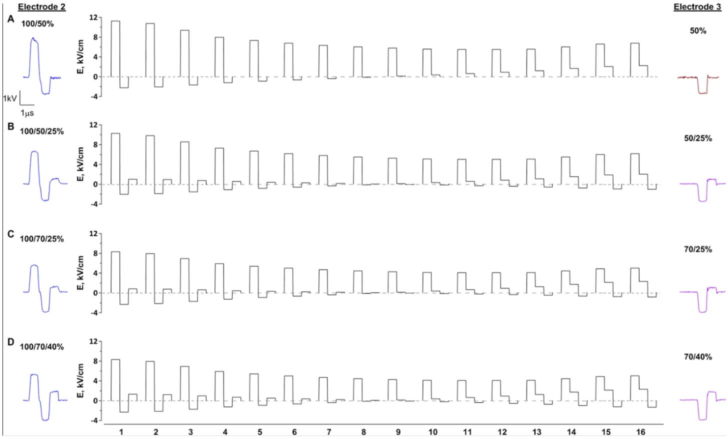

Figure 2.6.: A schematic overview of the superposition of two generated signals at different locations is depicted. On the left (blue) and right (red), the original waveforms are shown as generated at the electrodes. The distance between stimulating electrodes was divided into 16 segments, as indicated on the x-axis, with the target site at segment 8. Different pulse shapes are displayed on the y-axis. At segment 8, superposition should generate a unipolar wave capable of generating an action potential. Away from it, superposition should cancel out the original waveforms. [47]

To evaluate the theory of nsEP cancellation, researchers used dyed molecules to visualize electroporation, indicating promising spatial selectivity for the stimulation method [47]. Experimentation with different electrode array orientations and the potential development of algorithms to optimize pulse signals could further refine the technique [48]. Recent studies have also investigated the effectiveness of a variant called next-generation CANCAN (NG-CANCAN). In NG-CANCAN, all electrodes generate unipolar waves, strategically arranged to form a bipolar wave that cancels out everywhere except at the center. This modification simplifies equipment requirements and offers greater flexibility in adjusting pulse parameters such as shape and duration for each electrode [49].

Despite promising results, the methodology used to validate these findings relied on the uptake of dyed molecules through electroporation, and the underlying mechanism remains incompletely understood. Consequently, it cannot conclusively demonstrate the ability to generate APs without relying on electroporation. While nsEP shows potential for applications like targeted apoptosis of cells, its efficacy in AP generation is less certain. The short pulse duration may open ion channels without polarizing the surface membrane, potentially leading to AP generation. However, the precise mechanism and feasibility of this approach are still uncertain. Furthermore, producing kV ns pulses requires specialized equipment, limiting the widespread adoption of this technique.

2.1.4. TRANSCRANIAL ELECTRIC STIMULATION

For transcranial electric stimulation (tES), a low-intensity current (1-2 mA) is applied via an anode and cathode electrode positioned on the scalp. This current passes through the scalp and extracortical layers to reach the cortex, where it modulates the membrane polarity of neurons within the underlying tissue region. tES influences neuronal states through various current waveforms applied transcranially. The current can be applied in different ways: direct current stimulation (tDCS), which can be either anodal or cathodal, Alternating Current Stimulation (tACS) and transcranial Random Noise Stimulation (tRNS), as depicted in Figure 2.7. These current forms are capable of inducing changes in electrical activity both inside and outside neurons, thereby altering resting membrane potential and affecting firing efficiency but without generating action potentials [50, 51]. tES is a well-tested technique with few side effects, although pain may occur, which can be mitigated with appropriate protocols [51, 52].

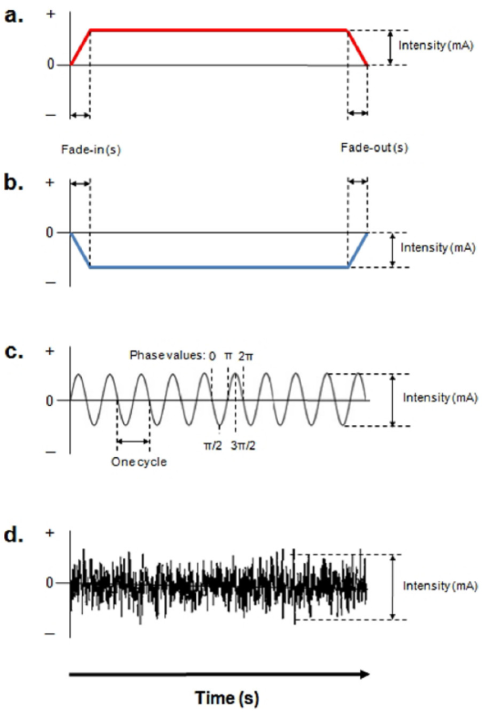

Figure 2.7.: (A) Anodal direct current stimulation. (B) Cathodal direct current stimulation. (C) Transcranial alternating current stimulation. (D) Transcranial random noise stimulation [50]

Anodal tDCS and tRNS have been found to increase neural excitability, while cathodal tDCS decreases neural excitability. Additionally, tACS can modulate excitability by entraining the desired firing frequency. However, multiple studies have revealed the complexity and nonlinearity of the induced effects. This complexity arises from the multitude of parameters available for experimentation [50]. Furthermore, the spatial resolution of tES is on the order of centimeters [50, 53].

While tES modulates neural activity, it lacks the capacity to directly excite neurons and exhibits limited spatial specificity [50, 51]. These characteristics are crucial for the vagus nerve stimulation project, where precise targeting and the ability to selectively excite specific neural pathways are essential. In contrast, tES finds greater utility in rehabilitation contexts, where its capacity to modulate neural impulses can aid in enhancing or suppressing desired motor or cognitive responses.

2.1.5. TRANSCRANIAL MAGNETIC STIMULATION

Transcranial Magnetic Stimulation (TMS) involves delivering brief high currents, typically in the range of several hundred amperes, through a coil to generate a magnetic field (B-field) [54]. The flux lines of the B-field run perpendicular to the plane of the coil, which is positioned tangentially to the scalp. The B-field induces an electric field (E-field) perpendicular to the B-field, capable of exciting neurons independently. Additionally, it elicits currents parallel to the coil's plane within the tissue, with increasing intensity from the coil's center (minimal current) to its periphery (maximum current), also capable of exciting neurons [55, 56]. Altering the coil's shape allows for adjustment of the spatial resolution to depth of stimulation ratio, offering some control over the stimulation's focus [54]. However, TMS's spatial resolution remains limited (in the order of cm) [57, 58].

One big advantage of TMS compared to tES is its capacity to generate currents within the tissue, resulting in less discomfort and ensuring that delivering a single pulse is relatively safe. However, TMS may exhibit slightly longer latency compared to tES [55]. With repetitive TMS (rTMS), effects may persist beyond the stimulation period. However, this technique also carries a risk of inducing seizures, which can be mitigated through adherence to appropriate safety protocols [55, 58].

While TMS is well-suited for investigating brain functions, its reliance on heavy and bulky equipment, along with components designed to handle high currents, makes it less suitable for applications such as vagus nerve stimulation.

2.2. STATE OF THE ART

This section explores the state-of-the-art techniques for cervical vagus nerve stimulation (CVNS). While vagus nerve stimulation can target both cervical and auditory regions, the focus here is exclusively on cervical stimulation devices.

Cervical vagus nerve stimulation is categorized into invasive and non-invasive methods. Invasive VNS involves surgically exposing the vagus nerve (VN) and wrapping a, commonly helical, electrode around it. This electrode connects via a lead to a pulse generator placed beneath the collarbone [9]. Non-invasive VNS, on the other hand, uses transcutaneous stimulation through electrodes placed on the skin.

Given the diverse functions managed by the VN, ensuring selectivity is crucial to minimize side effects. This is typically achieved through anodal blocking, fiber selectivity, or spatial selectivity [4, 9, 59]. Anodal blocking prevents action potentials in certain nerve fibers, allowing selective transmission [60]. Stimulating above the anodal block allows the transmission of only afferent signals, while stimulating below allows only efferent signals. This technique can target specific regions, such as stimulating the brain while reducing cardiovascular side effects by blocking efferent fibers. Fiber selective stimulation uses the fact that the VN contains three fiber types: A, B, and C. A fibers have the largest diameter and the lowest threshold, while C fibers have the smallest diameter with the highest threshold [13, 14]. By creating an electric field strong enough to activate A and some B fibers but not C fibers, selective stimulation can be achieved. Spatial selectivity is based on the theory that VN fibers are spatially organized by function. By targeting specific parts of the VN, only the connected organ or function is stimulated, reducing unwanted side effects [14].

2.2.1. INVASIVE DEVICES

Older invasive VNS devices required patient or caretaker activation of the device, using a magnetic key [61]. Modern devices, such as the AspireSR (Cyberonics) and Sentiva, use algorithms to detect changes in heart rate and predict seizures, automatically activating the stimulator to prevent seizures [9, 61–63]. These devices are approved for treating epilepsy and depression [9, 61]. Since the right VN contains more cardiac targeted nerves, the left cervical VNS is preferred to avoid cardiac effects [61]. The automatic seizure detection comes with slightly reduced battery life but also a higher quality of life [61, 62]. The Vivistim stimulator aids rehabilitation by allowing therapists to trigger VNS during motor tasks, enhancing motor function recovery [9, 64]. For heart failure treatment, the CardioFit system uses a transvenous lead in the right ventricle and a nerve stimulation cuff around the right VN, connected to an implanted pulse generator. This system minimizes the activation of A-fibers by using a multi-contact cuff electrode with anodal blocking, reducing side effects while activating parasympathetic efferent B-fibers [9, 60, 63].

2.2.2. NON-INVASIVE DEVICES

Invasive VNS involves surgical risks and does not always guarantee successful seizure control [65]. Non-invasive VNS, although limited in its capabilities compared to invasive VNS, completely removes this risk.

Currently, the only non-invasive cervical VNS device, approved for treating episodic cluster headaches and migraine, is the GammaCore [9, 61, 63, 66–68]. The GammaCore features two electrodes that are placed on the skin's surface by the patient, see Figure 2.8 [9]. One electrode serves as an anode with a 1 ms pulse, comprising of a 5 kHz sine wave repeated at 25 Hz, capable of delivering a current up to 60mA. While the other electrode acts as a cathode [7, 63, 69]. These electrodes generate a current flow that reaches the VN, selectively activating A and some B fibers without affecting C fibers [7, 70]. Adverse events are generally mild or moderate, including local discomfort, skin irritation, muscle stiffness, and dizziness

[60]. Skin irritation due to current density at the electrode-skin interface is a common side effect, as described in section 2.1.1.

There are other TENS devices designed for placement on the neck, like the Gentle Stim and GentleAce [71, 72]. These devices use interfering high-frequency waves to create 50 Hz amplitude modulation, similar to TI, which should be more comfortable than pulsed currents [71, 73]. They focus on activating muscles to improve swallowing and have potential for VNS. Wang et al. successfully tested this, demonstrating increased motor-evoked potentials, though the mechanism of activation remains experimental and not fully understood for this use case [72]. The activation mechanism is likely similar to that of GammaCore.

The scarcity of non-invasive VNS devices and other mechanisms for creating selectivity is probably due to the distance between the electrodes and the VN, as well as the relatively small diameter of the VN compared to this distance. Achieving spatial selectivity would require a highly focused E-field. Even if technically feasible, variations in human anatomy, such as fat tissue distribution, make it unlikely to achieve spatial selectivity without detailed patient-specific scans [4]. Therefore, fiber selectivity, as employed by GammaCore, remains the most viable approach. The biggest downside of this approach is the need for patient involvement, which complicates automatic seizure detection [61].

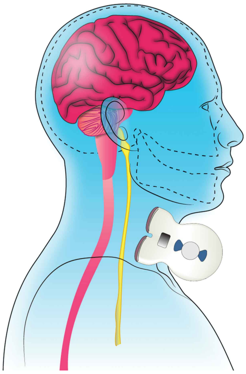

Figure 2.8.: The GammaCore and its placement against the neck. The vagus nerve is depicted as yellow [7]

2.2.3. ADVANCEMENTS IN STIMULATION SELECTIVITY

As described above, the threshold of nerve fibers is dependent on their diameter. As the current increases, fibers are activated in the order of A, B, and C [13]. Since the E-field decreases over distance, successful activation also depends on the proximity of the fibers to the stimulation source [13]. Fiber selectivity, as previously mentioned, is one method to achieve higher selectivity. It has limitations regarding the degree of selectivity that can be achieved, as it will always stimulate all the fibers with a certain threshold or lower, even if they have different functionalities. Therefore, other methods like spatial selectivity are also being explored. There is a common agreement that increased selectivity of VNS can mitigate side effects and open up VNS for other applications [4, 5, 10, 11].

Buckshot et al. tested the viability of flat electrodes instead of the generally used helical electrodes to see if they could be used for VNS without compromising effectiveness [74]. The benefits would be easier manufacturability and implantation. Despite the less uniform current distribution, the flat electrodes were capable of stimulating all large-diameter fibers used for epilepsy treatment VNS, equivalent to the helical ones [74]. This suggests that the decrease in current density with distance is not a big issue for fiber-selective stimulation on the scale of the VN.

Cardiovascular applications can greatly benefit from selective VNS because they require the recruitment of smaller diameter fibers that innervate the heart [4, 11]. The use of different pulse shapes like trapezoidal or burst stimulation can selectively activate smaller fibers, which is beneficial for cardiovascular applications [75–78]. This can also be achieved using anodal blocking to inhibit afferent fibers and prevent side effects [4, 79].

Pitzus et al. developed a method to establish the functional topography of the VN [59]. They believe that spatially selective stimulation of the VN can modulate a target function without altering other physiological functions, whereas fiber selective stimulation is limited by the activation of large diameter fibers versus small fibers [59]. Ordelman et al. were the first to focus on spatially selective VNS, achieving almost double the efficacy in cardiac modulation compared to conventional VNS using a multi-contact cuff electrode with bipolar stimulation in pigs [80]. Plachta et al. used a multi-contact cuff electrode with selective tripolar stimulation to show that spatially selective VNS could lower blood pressure by up to 40% in rats [81].

Dali et al. experimented with spatially selective VNS on sheep using a finite element model to optimize stimulation parameters. They identified the "transverse tripolar + ring" (TTR) configuration as the optimal balance between selectivity and efficiency, reducing side effects by 62% compared to non-selective VNS [11]. Aristovich et al. further optimized geometrical parameters in a sheep model, achieving selective reduction of respiration rate by 90% and heart rate by 27% [6]. Jayaprakash et al. designed a multi-contact cuff electrode to match the anatomical organization of vagal fibers in swine, enabling fascicle-selective VNS [15]. This selective stimulation resulted in distinct physiological responses, such as changes in muscle activity, cough reflex, breathing, and heart rate, corresponding to the documented fascicular organization. This demonstrates that vagal fibers are organized by function and can be selectively activated, improving the precision and effectiveness of VNS therapy [15]. Ravagli et al. combined spatially selective VNS with Fast Neural Electrical Impedance Tomography in a single electrode. They demonstrated that spatial selectivity is possible using current steering and that imaging of the E-field can be done using the same electrodes in a single nerve cuff [82].

The use of multi-contact electrodes described above for increased spatial selectivity is used already in other fields like deep brain stimulation and is known as current steering [83, 84]. By changing the charge applied to different contact points, it is possible to steer the E-field and create a virtual electrode [85]. Figure 2.9 shows that simply changing the ratio of the charge applied to two electrodes can steer the E-field in a certain direction [83, 84]. This can be greatly beneficial in the case of spatially selective VNS.

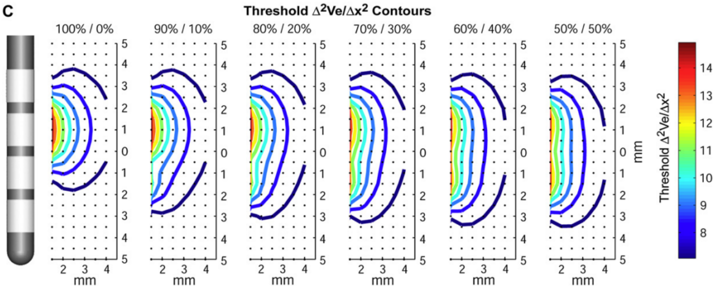

Figure 2.9.: Current steering using stimulating two electrodes with different intensities. Changing the ratio of intensities between the electrodes allows for steering of the E-field. [83]

Kilohertz Electrical Stimulation (KES) block, demonstrated by Patel et al., applies an electrical stimulus of at least 5 kHz to inhibit action potential propagation. Traditionally, KES aimed to block the entire nerve for directional selectivity, but Patel et al. showed it could also achieve fiber-selective stimulation [86, 87]. However, practical advancements over anodal block remain unclear since improper parameter selection can induce severe nerve damage [87].

To conclude, even though approved VNS devices typically use whole nerve activation, differences in fiber thresholds mean that some kind of selectivity is possible. To minimize side effects and explore new applications for VNS, stimulation devices need to be developed that are even more selective. The most promising approach involves combining spatial selective stimulation with fiber selective stimulation or blocking. Using spatial selective stimulation, only the desired area of the VN is targeted, thereby limiting side effects to those caused by fibers in that specific area. Fiber selectivity or anodal block can then further reduce these side effects.

In terms of non-invasive VNS, achieving spatial selectivity to a degree that significantly reduces side effects seems unlikely due to the distance between the electrodes on the skin's surface and the VN, as well as the variability in morphology between patients. However, non-invasive VNS can still be improved by reducing skin irritation and using fiber selectivity to minimize unwanted activation.

2.3. LITERATURE DISCUSSION

Examining the various stimulation techniques, it becomes evident that tES and TMS are unsuitable for non-invasive VNS. For tES, the spatial resolution of centimeters is insufficient compared to the size of the VN, and this method modulates firing rates rather than generating APs. TMS, which uses high currents and a large magnetic coil to induce APs, is impractical for the space available around the neck. TENS, although capable of creating APs, is limited by its spatial selectivity. Smaller electrodes can enhance selectivity but increase patient discomfort due to higher current density.

TI and nsEP exhibit greater spatial selectivity and could potentially improve non-invasive VNS. However, the mechanism by which nsEP induces APs is uncertain, necessitating caution, especially with the VN's small cross-sectional area, where even spatially selective activation could cause damage if done wrong. TI appears to be a viable option, assuming blocking and tonic firing outside the target area is acceptable. Nevertheless, the potential increase in selectivity with TI is difficult to determine from currently available data. Given anatomical differences in humans and the VN's small size relative to electrode distance, achieving enhanced spatial selectivity seems not yet technically feasible. The focus should thus shift to fiber selectivity and reducing patient discomfort.

During this review, a correlation was found between nsEP and TI using the SD curve. The SD curve indicates that nsEP requires a high electric field to compensate for the ultra-short stimulation pulse. whereas for TI, the carrier wave amplitude is too low for the pulse duration, but the slower envelope amplitude suffices. This led to the novel idea of utilizing the SD curve differently to achieve higher spatial selectivity. By identifying a point on the SD curve and distributing the minimum pulse duration across multiple electrodes, the electric field in the target area would be sufficiently stimulated to generate an AP, while in other areas, the combined electric field and pulse duration would be inadequate, see Figure 2.10a.

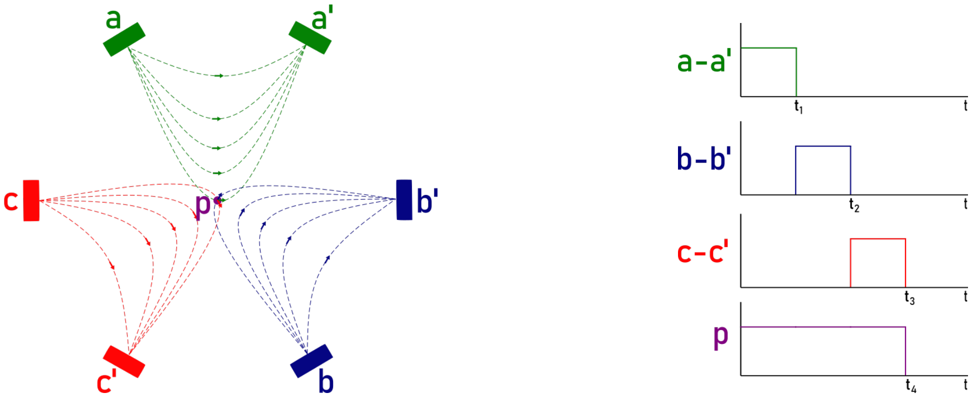

(a)

(b)

Figure 2.10.: Impression new stimulation technique

2.4. THESIS OBJECTIVE AND APPROACH

Based on the literature review, a novel stimulation technique has been conceptualized. This technique utilizes the strength-duration curve to identify the threshold current and corresponding pulse duration. By distributing this duration across multiple electrodes, it creates a spatially and temporally dependent electric field. The hypothesis is that this stimulation technique enables spatially selective activation. The primary objective of this thesis is to establish a simulation framework capable of simulating temporally dependent stimulation from at least two electrodes. This will be used to assess whether the generation of a temporally and spatially dependent electric field can enhance spatial selectivity for stimulation of the central vagus nerve.

3

METHODS

During the literature review, a novel method for creating spatial selectivity in nerves was proposed to enhance cervical vagus nerve stimulation (CVNS). This technique leverages the strength-duration (SD) curve to identify a specific pulse duration and corresponding threshold current. Subsequently, the pulse duration is distributed across multiple electrodes to generate a temporal electric field (E-field). According to the hypothesis, this approach can induce spatial selectivity within the nerve. This novel technique, which incorporates a temporal component to current steering, is referred to as Temporal Current Steering (TCS).

This chapter describes the methods developed to validate TCS and compare it to existing invasive and non-invasive VNS techniques to assess its potential advantages. The first step involves creating a simulation environment capable of modeling the E-field produced by multiple electrodes and its effect on nerves. Due to the nonlinearity of the nerve membrane, determining an activation pattern that maximizes spatial selectivity is challenging [88, 89]. Therefore, an optimization algorithm is needed to utilize the simulation environment to refine stimulation waveforms for optimal spatial selectivity.

3.1. SIMULATION ENVIRONMENT

To determine the viability of TCS as a stimulation option for the CVN, a simulation is used. NEURON [90] is utilized for simulating the behavior of neurons. Python serves as the interface with this program. The subsequent sections will elaborate on the programs and models used.

3.1.1. NEURON

NEURON is a program designed to simulate individual neurons and neural networks [90]. It effectively solves the differential equations governing membrane potential along the axon to determine whether an action potential is generated. Originally written in HOC, a programming language that facilitates the construction of complete neural networks with individual axons and somas, NEURON has since been updated to support Python, a more modern and widely used programming language. Python compatibility allows for importing and exporting values to NEURON, leveraging Python's capabilities for calculating and displaying results. This integration also enables running the complete simulation via a single Python script, enhancing efficiency and ease of use.

To simulate the E-field for extracellular stimulation, two primary methods are employed. One method involves creating a finite element model of the surrounding tissue to calculate the changing E-field along the axon over time. This data is then imported into the simulation, as described by [7]. Alternatively, the surrounding tissue can be modeled more simply, often as homogeneous and isotropic, allowing for the calculation of the transfer resistance and the resulting membrane potential along the axon, as described by [36, 91]. While creating a finite element model provides a more realistic representation of the stimulation, the second approach enables the entire simulation to be executed within a single program. Given that the primary goal of this thesis is to validate the stimulation method, fast iteration is prioritized, making the second method the preferred choice for the simulation.

MRG MODEL

For the fiber model, a tested and validated model was employed: the McIntyre-Richardson-Grill (MRG) model. This model represents myelinated axons using a double cable approach, which allows for separate electrical representation of the myelin sheath and the underlying internodal axolemma [92]. The MRG model is composed of segments, and extracellular stimulation can be applied by calculating the extracellular potential at each segment. Assuming a homogeneous and isotropic medium, this calculation can be easily performed for one or multiple point sources using transfer resistance (3.1). Given that the fibers targeted for stimulation are generally myelinated [13] [93], and the MRG model is designed for extracellular stimulation of myelinated fibers, it was chosen for this project. Furthermore, the MRG model has been widely used in simulations for validating both Transcutaneous Electrical Nerve Stimulation (TENS) and extracellular stimulation [33, 36, 83].

$$ex = is_1 * R_{x1} + is_2 * R_{x2} + ... + is_n * R_{xn} \tag{3.1}$$

Where:

$ex =$ extracellular potetnial

$is_n =$ Stimulation current electrode$n$

$R_{xn} =$ Transfer resistance electrode$n$

$n =$ Number of eectrodes

The CVN consists of A, B, and C fibers, with around 80% being C fibers [13]. A fibers have diameters ranging from 1 to 22 μm, while B and C fibers have diameters of $\leq 3\mu$m [13, 94]. Havton et al. reported that the average fiber diameter in the CVN is $1.43 \pm 0.08\mu$m [94]. An axon diameter of 5.7 μm was chosen as it was closest to the reported diameters in the CVN.

When an electrode is positioned such that the E-field remains strong at the edge of the fiber, activation can occur at the edge rather than at the point where the E-field is strongest (i.e., the shortest distance between the electrode and the fiber). This edge effect is evident in Table 3.1, showing that only when the electrode is 3.5 mm away from the edge of the fiber does the expected node, located at 3.5 mm, activate first.

The fiber model is originally 10 mm long. If the axon is placed 36 mm from the skin surface, with electrodes spaced at 40 mm as in the GammaCore device [7], the fiber would need to be elongated at least eight times, and probably more, to eliminate the edge effect. This elongation would increase the simulation time approximately 11-fold, from 0.45 seconds to 5 seconds, which is too long for the planned simulations. Therefore, the axon was placed at a distance of 3 mm, and the fiber was elongated two times. This adjustment increased the simulation time approximately two-fold, from 0.45 seconds to 0.95 seconds, ensuring the elimination of the edge effect. The 3 mm distance was chosen to keep the simulation time manageable and maintain low values for stimulation amplitudes and coordinates used in the calculations. This distance is also used by Warman et al. for experimentation with extracellular stimulation [95].

Table 3.1.: Table shows the electrode locations and the first node that generates an action potential, simulated using the original MRG model with a length of 10 mm under extracellular stimulation.

Electrode coordinate (x,y,z) [mm]	First activated node	Node location [mm]
(0.5, -3, 0)	node[0]	0
(1, -3 , 0)	node[0]	0
(1.5, -3, 0)	node[0]	0
(2, -3, 0)	node[0]	0
(2.5, -3, 0)	node[0]	0
(3, -3, 0)	node[0]	0
(3.5, -3, 0)	node[7]	3.5

3.1.2. PYTHON

As mentioned, NEURON is available as a Python module, which facilitates the use of a wide range of analysis tools available in Python to improve the simulation set-up. Therefore the simulation was configured in Python and only alterations to the MRG model were done in HOC.

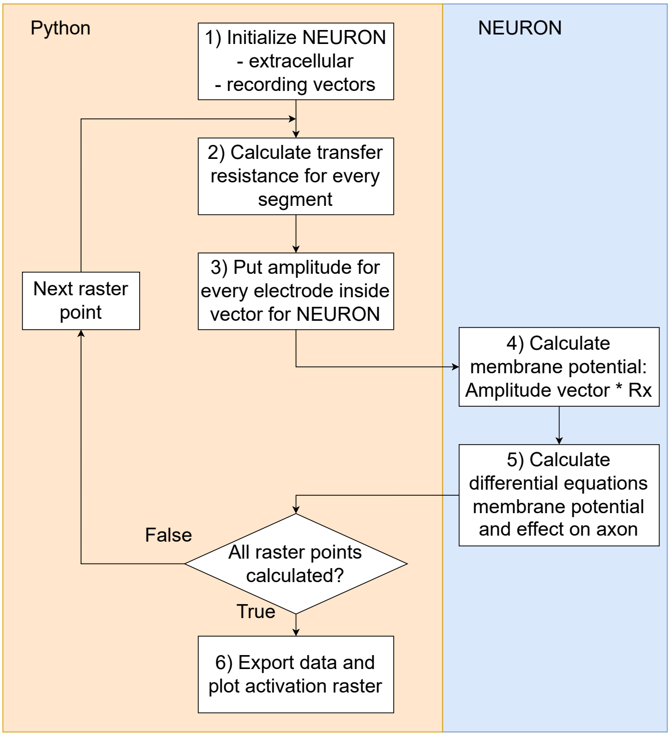

Figure 3.1.: Flowchart interdependence of Python and NEURON code within the main simulation for generation of an activation map

As depicted in Figure 3.1, the first step involves initializing NEURON, which includes setting up the MRG model and adding the required variables for extracellular simulation, as well as vectors to record the eventual output. In this case, the output provides the amplitude vector of the membrane potential at every node. Subsequently, the transfer resistance for a unit charge is calculated for every electrode at every segment, as outlined in (3.2) and (3.3).

$$r = \sqrt{(x - \mathrm{seg\_x})^2 + y^2 + (z - \mathrm{seg\_z})^2} \tag{3.2}$$

$$R_x = \frac{1e-3}{4\pi\sigma_e r} \tag{3.3}$$

Where:

$r =$ Radius electrode to segment

$x, y, z =$ Electrode location

seg_x, seg_z = Segements location

$R_x =$ Transfer Resistance per unit charge

$\sigma_e =$ Extracellular conductivity

The conductivity σ_e has been selected as 3e-07 [S/μm], consistent with Warman et. al's work and used by others [92, 95].

In the subsequent step, the predefined waveform vector (3.5) is extracted from the stimulation vector (3.4). The stimulation vector contains for every electrode the stimulation waveform. If the length of the waveform vector corresponds with the time step of the simulation, the wave simulated is identical to the waveform vector. If the waveform vector is shorter than the simulation timestep, the amplitudes are extended creating square waves. Then, within NEURON, the amplitude vectors are multiplied by the transfer resistances corresponding to the electrodes, which are subsequently summed to calculate the extracellular potential (3.1) at every segment due to the electrodes. NEURON then proceeds to compute the differential equations and the membrane potential, which can be utilized to determine whether activation has occurred or not. The stimulation time was set to 0.2ms as this is the same as the wave length of the 5kHz stimulation wave of the Gammacore [7, 96] and other invasive devices also use 0.2ms or pulse width in the same range [14, 30].

$$\text{Stimulation Vector} = [el_1, el_2, ..., el_i] \tag{3.4}$$

$$\text{Waveform vector} = el_i = [amp_1, amp_2, ..., amp_n] \tag{3.5}$$

Where:

Stimulation Vector = Vector containing the waveform vector for each electrode

$i =$ Number of electrodes

$el =$ Vector containing the amplitudes of the stimulation waveform of one electrode

$n =$ Number of amplitude changes

To get the spatial selectivity of a specific stimulation setup, a raster was created with the radius of the thickness of the CVN. Given that the MRG model is configured as a single axon positioned at z = 0, y = 0, and extending along the x-axis, the most effective approach to visualize this selectivity is achieved by relocating the electrodes. This ensured minimal disruption to the validated MRG model. By adjusting the electrode positions relative to the axon while maintaining the same stimulation parameters, a raster could be generated depicting points where activation occurs or does not occur, as outlined in Figure 3.2.

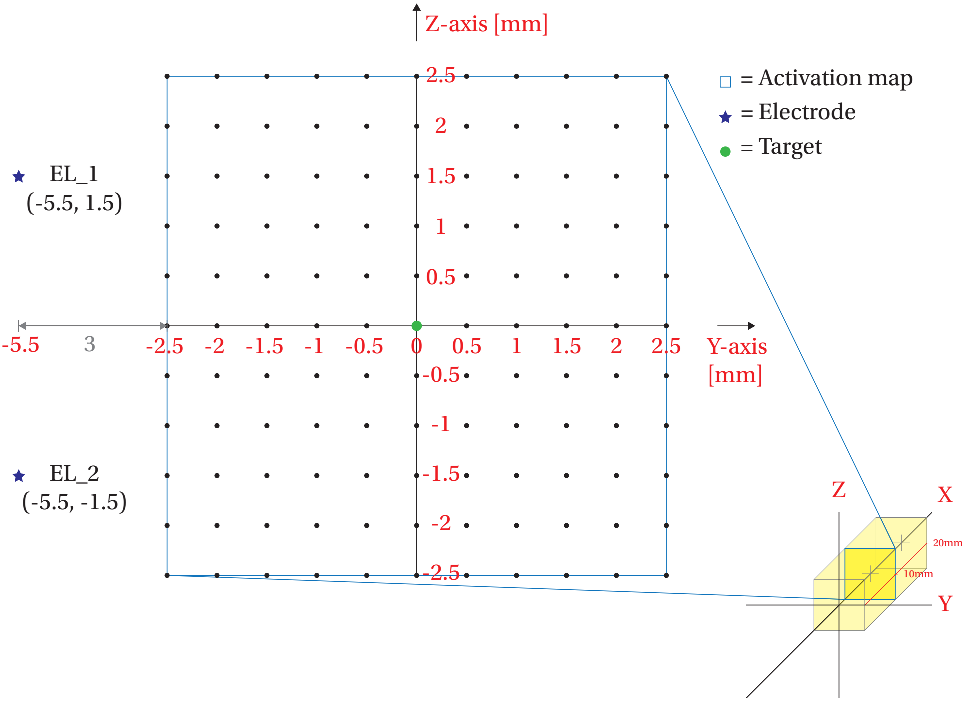

Figure 3.2.: Representation of the simulation setup

3.2. IMPLEMENTATION OF OPTIMIZATION ALGORITHMS

The non-linearity of neurons [18, 89] poses a challenge in determining the optimal stimulation pattern or even defining what the pattern should resemble. Therefore, optimization algorithms are employed to achieve the highest spatial selectivity in activation. Wongsarnpigoon et al. utilized a Genetic Algorithm (GA) to find the energy-optimal waveform shape for neural stimulation [89]. They used NEURON with the MRG model for simulations, making it applicable to this problem set as well. Particle Swarm Optimization (PSO) serves as an alternative to GA for optimizing stimulation parameters [97–99]. Both algorithms will be further explained in this section.

3.2.1. GENETIC ALGORITHM

A genetic algorithm operates on the principle of survival of the fittest [100]. The Python implementation of this algorithm follows the flowchart outlined in Figure 3.3. Initially, a population is created, consisting of genomes. Each genome is filled with a stimulation vector, as shown in (3.5). Subsequently, the simulation is executed for every genome. The performance of each genome is evaluated using a fitness function (3.6).

The fitness function is a penalty function based on the excitation of undesired points, weighted by the distance to the target location (0,0). Additionally, a high penalty is added if the target location is not excited. As a result, high spatial selectivity results in a low fitness score. To prevent the algorithm from converging too quickly, the fitness results can be linearized to prevent good, early results from dominating the population [100]. Early convergence is undesirable as the algorithm has not yet explored other waveforms, and better solutions may be missed.

$$Fitness = \begin{cases} \sum_i R_i^3 Excitation_i + penalty & \text{if Excitation}_{(0,0)} = 0 \\ \sum_i R_i^3 Excitation_i & \text{otherwise} \end{cases} \tag{3.6}$$

Where:

$R =$ radius of point i to the desired excitation point

$Excitation = 1$ if point excited or 0 if not

$i =$ The number of points in the stimulation raster

To discourage the solution where EL_1 is stimulating while EL_2 is zero or reversed, the radius was experimentally set to $R^1, R^2 \text{and} R^3$. A higher exponent results in a greater penalty at the edges, which would activate in the described scenario. Preliminary tests indicated that increasing the exponent indeed produced the desired effect. After R^3, higher exponents were not tested due to the rapidly increasing fitness values.

In addition to the fitness function described above, a parameter called "linelength" can be added to promote less complex solutions. The larger the amplitude swings in the waveform, the larger the linelength (3.7). For each genome, the waveform vectors are combined into one vector. The linelength is then calculated over this vector and normalized, then multiplied by a fixed value and added to the fitness score. The maximum linelength is not sufficient to cause a waveform with higher spatial selectivity to receive a worse fitness score than a waveform with lower spatial selectivity. However, it does favor genomes with less complex shapes when spatial selectivity is the same.

$$Linelength[i] = \sum_{n=0}^{m} |amp_n - amp_{n-1}| \tag{3.7}$$

Where:

$i =$ Number of genomes

$m =$ Number of amplitude changes

$amp_n =$ The amplitude at point n

After all the fitness values are calculated, a new population is generated. In this new population, old genomes are combined at random points, a process called cross-over [100]. The genomes chosen for cross-over are selected randomly, but with a higher probability for better-performing genomes. Over multiple generations, some mutations, alterations to existing genomes, are introduced to continue exploring new waveforms.

The continuous updating of the population, with a bias towards better-performing genomes and their combinations, should result in optimal spatial selectivity. By the end of the program's execution, this approach aims to achieve a state where only the desired point is activated, reflecting the highest spatial selectivity.

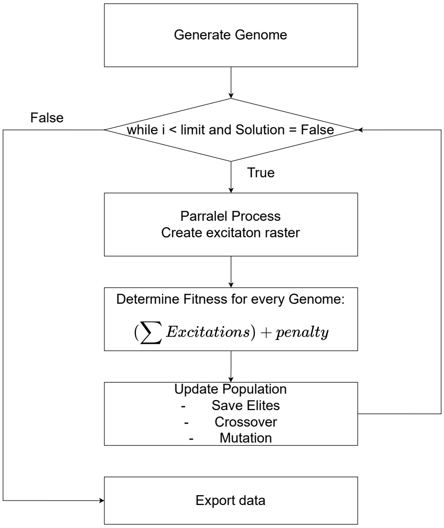

Figure 3.3.: Flowchart Genetic algorithm

3.2.2. PARTICLE SWARM OPTIMIZATION

Particle Swarm Optimization (PSO) is inspired by the collective behavior observed in certain animal groups, such as flocks of birds [101]. Similar to Genetic Algorithms (GA), PSO begins with the creation of a swarm, analogous to a population. Each particle within the swarm is initialized akin to genomes in GA. Subsequently, simulations are executed to generate the activation patterns and corresponding fitness values. These are evaluated following the same procedure to GA.

During iterations, each particle maintains its own best-known position (personal best) and monitors the overall best position discovered by any particle in the swarm. In each iteration, the particles adjust their positions based on the new velocity (3.8). Initially, the algorithm emphasizes exploration by assigning a higher weight to the current velocity when computing updates. As iterations progress, this weight is gradually reduced, encouraging particles to converge towards the overall best solution found by any particle in the swarm [101].

$$v_{d_{i,t+1}} = \omega \cdot v_{d_{i,t}} + c1 \cdot \text{rand} \cdot (p_{d_{i,t}} - x_{d_{i,t}}) + c2 \cdot \text{rand} \cdot (p_{d_{g,t}} - x_{d_{i,t}}) \tag{3.8}$$

Where:

$v_{d_{i,t+1}}$ = updated velocity for dimension d of particle i at time $t+1$

$v_{d_{i,t}}$ = current velocity for dimension d of particle i at time t

$p_{d_{i,t}}$ = best position found so far for particle i in dimension d at time t

$x_{d_{i,t}}$ = current position for particle i in dimension d at time t

$p_{d_{g,t}}$ = best position found so far by any particle in dimension d at time t

$c1, c2$ = constants

ω = Intertia weight, scaled down over the number of iterations

rand = a random value between 0 and 1

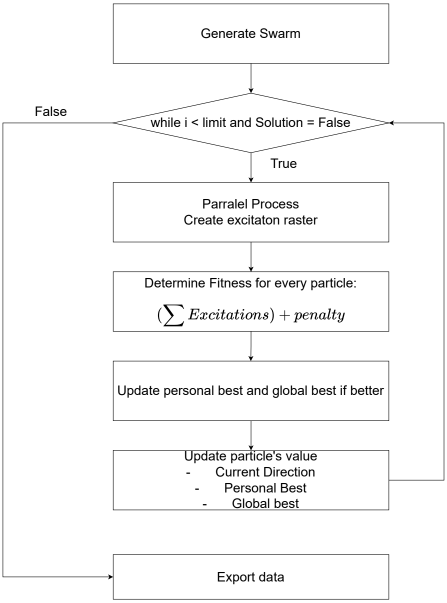

Figure 3.4.: Particle Swarm Optimization flowchart

In essence, PSO involves particles starting from different positions and collectively moving towards a shared optimal solution. The process incorporates randomization to explore various options, potentially improving fitness values. As particles discover better solutions, all adjust their paths accordingly. Over time, individual contributions diminish to promote convergence towards the globally best solution explored by the particles. Peña et al. applied this method to optimize electrode configurations and amplitudes in an electrode array, enhancing spatial selectivity for deep brain stimulation [102].

3.3. SIMULATION PARAMETERS AND OPTIMIZATION

The creation of the activation raster, which depicts spatial selectivity, is a time-intensive process, particularly when conducting numerous simulations to pinpoint the optimal stimulation pattern using optimization algorithms.

Achieving convergence requires a large number of iterations with these optimization algorithms. Grill et al. conducted up to 10,000 iterations, finding that for pulse widths smaller than 0.5 ms, convergence within 1% was achieved within 5,000 iterations, with discernible a waveform observed from 2,000 iterations onwards [89]. Therefore, the target minimum iteration count was set at 2,000. Furthermore, multiple simulations should be run, a so called multistart, to ensure that the global minimum is found and not a local minimum. This is crucial given the vast number of unique genome configurations available due to the numerous free parameters involved. The number of iterations and multistart require a lot of processing time where only limited is available. Using the DelftBLue super computer [103] allowed for a maximum of 100 hour runtime and 46 cores per simulation. Parameter optimization and parallelization of the code need to make sure these resources are used as efficiently as possible.

In Figure 3.2 the final simulation setup can be seen. Two electrodes were used for the stimulation as it is the least amount that can validate TCS and more would increase the available parameters making optimization even more cumbersome. The length of the axon and the distance of the electrodes to the raster also have been chosen for simulation optimization as described in subsubsection 3.1.1. The electrodes are placed orthogonal which creates intersecting fields strongest at the crossectional plane of the CVN. In contrast to the GammaCore where the electrodes are placed parallel [7], which creates a strong E-field at two different locations in the VN among its length, which is not desirable for TCS.

The raster size was optimized to range from -2.5 to 0.5 mm in the y-direction, as points beyond 0.5 mm rarely activate due to electrode placement at y = -5.5 mm and the target point being at y = 0 . This optimization reduced calculation time greatly by eliminating unnecessary calculations. The activation rasters in this study illustrate the complete raster plotted with the obtained results to provide a comprehensive view.

Simulation time for each activation raster point was predominantly influenced by the time step (dt) used during calculations. A smaller dt enhances accuracy but extends simulation duration. A dt of 0.001 ms was chosen, as it showed minimal threshold value change (less than 1%) compared to smaller increments, as detailed in Table 3.2.

To further optimize efficiency, parallel processing was implemented. Each iteration of the algorithms involved simultaneous calculation of multiple rasters across cores, ensuring optimal utilization of available processing power.

For both the GA and PSO, the efficacy of the optimization heavily relies on

Table 3.2.: Electrode location 10000-5500 1500 Stimulation time 02ms The change in Threshold value is with respect to the next higher dt

dt	Threshold value	Change in Th	Stimulation time
0.0001	-7388.96	-	10.72s
0.001	-7404.39	0.2%	1029.52 ms
0.01	-7609.66	2.8%	97.77ms

the proper tuning of parameters. Tuning these parameters can be a substantial undertaking. Since standard libraries could not be used because of the integration of NEURON to generate the fitness, time was invested in writing the algorithms in Python. Standard parameter values from [100] and [101] were used. In section 4.2, variations on these parameters for both GA and PSO are tested, and the best-suited variant for TCS will be used for the multistart simulation.

4

RESULTS

To validate the concept of TCS, first, the simulation code was tested against experimental data used to validate the original MRG model. Subsequently, a trial run with two different optimizer algorithms was analyzed to justify the choice of the algorithm selected for the multistart. Following this, the results of the multistart were compared with each other and analyzed to determine a potential optimal stimulation pattern. Finally, TCS results were compared to those of single electrode stimulation and direct current steering (DCS) obtained using the same simulation environment.

4.1. MODEL VALIDATION

The extension of the MRG model, selection of dt, inclusion of extracellular stimulation with multiple sources, and the implementation of the model in Python created a simulation setup distinct from the original MRG model. Therefore, it is crucial to verify the continued validity of the MRG model. In the original paper describing the model, validation was performed by comparing the threshold values at various distances with experimentally found threshold values [92].

In Figure 4.1, both the original distance versus threshold plot (Figure 4.1a) and a new distance versus threshold plot created with the modified MRG model using Python (Figure 4.1b) are shown. The new plot falls within the range of the experimental data, meeting the criteria for model validation as described by [92].

Discrepancies between the original and new simulated plots could arise from differences in measurement points, methods of determining the threshold, the transfer of stimulation amplitude to the simulation, or the extension of the axon lengthwise. Despite these differences, the close alignment of the new plot with experimental data suggests that the MRG model remains valid in this context.

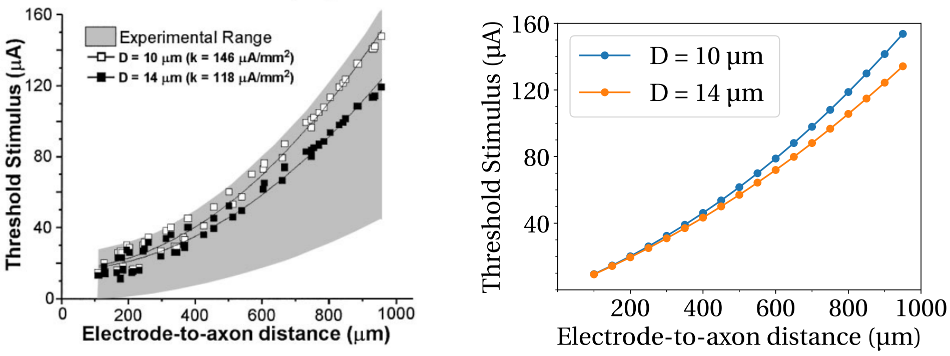

(a) (b)

Figure 4.1.: A) Original Distance vs Threshold plot with experimental and simulation data 100 μs pulse [92]. B) Distance vs Threshold plot created with MRG model using python

4.2. GENETIC ALGORITHM VS PARTICLE SWARM OPTIMIZATION

The GA and PSO are employed to optimize the given input range for achieving the highest spatial selectivity. Given the numerous possible amplitude combinations and limited processing power, finding a global minimum is challenging, making an effective starting population crucial. This was evaluated using the multistart simulation. A trial run of both the GA and the PSO was conducted with variable parameters, as detailed in Table 4.1, to determine the optimal algorithm for the multistart. Due to limited computational power and the high demand of computational resources by the multistart simulation, which requires 100 runs, only a single run was performed for each variable configuration.

The primary goals were to identify the algorithm that resulted in the lowest fitness and to evaluate the run time, as each run was limited to 100 hours. For the multistart simulation, it was essential that all runs be completed within this time frame to properly save all data. Initial trials indicated that the time for one generation could vary, necessitating a long run to obtain an average run time. All starting populations were created with fixed values, as detailed in the 'Starting population amplitudes' column of Table 4.1. For the PSO, the amplitudes were free to move in any direction after initialization because the optimization naturally explores in the direction of the current and best values (subsection 3.2.2). This approach prevents the generation of unrealistic waveforms, such as those where the amplitude is tenfold the threshold current, provided the starting population is realistic. In contrast, for GA, the crossover and mutation processes can result in a new population that is extremely different from the previous one (subsection 3.2.1). Leaving the GA unbounded creates a nearly infinite number of possibilities, making convergence during the multistart unlikely and producing unrealistic waveforms (as observed with GA V4). To limit this behavior the amplitudes were constrained to the values shown in Table 4.1.

Table 4.1.: Table containing the parameters for the initial optimization algorithms. PSO V1: Variation on swarm update. PSO V2: Standard update. PSO V7: Standard update. GA V3: Optimizer only used for calculation fitness. Optimized values rounded to {0, -th or th}. GA V4: Amplitudes unrealistic high. GA V5: Positive amplitudes free to change in any value. Negative values constricted. Genome scaling: multiplications of the waveforms unit the target is stimulated.

Algorithm	#iterations	Fitness	Starting population amplitudes	Amplitude range	Genome scaling	Linelength	Linear scaling	Elites
PSO V1	2000	60	{-2*th, -th, -.5*th, 0, 0.5*th, th, 2*th}	free	no	no	no	N/A
PSO V2	2000	63	{-2*th, -th, -.5*th, 0, 0.5*th, th, 2*th}	free	no	no	no	N/A
PSO V7	1800	62	{-2*th, -th, -.5*th, 0, 0.5*th, th, 2*th}	free	yes	yes	no	N/A
GA V3	1973	73	th, -th, 0	{0, th, -th}	yes	no	yes	no
GA V4	1897	None	th, -th, 0	{0, th, free}	yes	no	yes	8
GA V5	2000	72	th, -th, 0	{0, th, +free}	yes	no	no	8

In six trial runs, PSO consistently outperformed GA. An explanation for this is that while GA explores a wider range of waveform possibilities, it still covers a limited number of options due to processing time constraints and lacks efficient optimization of high-performing waveforms. PSO, on the other hand, optimizes the starting population more effectively rather than generating entirely new patterns. Among the PSO trials, V1 performed the best with a fitness value of 60, closely followed by V7 with 62 and V2 with 63. Despite V1's superior performance, it used an altered population update method where the particles would not take into account their current position. The slight increase in spatial selectivity over V2 and V7 was not sufficient to justify using an experimental update method for the entire multistart simulation. V2 and V7 were identical in all aspects except for the inclusion of linelength and Genome scaling in V7. Linelength, as described in subsection 3.2.1, promotes simpler waveforms if the spatial selectivity is the same. Given V7's better performance and the importance of linelength, PSO V7 was chosen as the algorithm version for the multistart.

To confirm the importance of the starting population in finding the best solution with limited resources, a multistart approach was taken. This involved running the experiment multiple times to see if the outcomes consistently converged to the same value, which is the desired result. If not, it indicates that the starting population plays a crucial role in finding the best solution with limited processing power.

4.3. RESULTS MULTISTART

A total of 98 simulations were conducted using identical parameters as PSO V7. The only difference among these iterations was the composition of the initial population, which was randomly generated for each run. The waveform vectors were populated with values randomly selected from the set {-2th, -th, -.5th, 0, 0.5th, th, 2th}. This ensured controlled variation of the waveform amplitudes, from where exploration could start. Each simulation extended up to 2000 iterations, constrained by the available processing time on the server.

4.3.1. TRENDLINE FITNESS

To assess the algorithm's performance, the change in fitness value for each run is plotted against the number of iterations. As noted, the inclusion of linelength in the fitness evaluation does not promote or demote results based on spatial selectivity but can promote simpler waveforms when spatial selectivity is the same. The normalized linelength is calculated at each iteration and can change depending on the other waveforms in the population. This introduces minor fluctuations in the fitness values since (unfiltered figure in Appendix A), but the overall trend reflects the optimization process. For clarity, a low-pass filter has been applied to smooth out these fluctuations caused by linelength. The filtered fitness values are depicted in Figure 4.2.

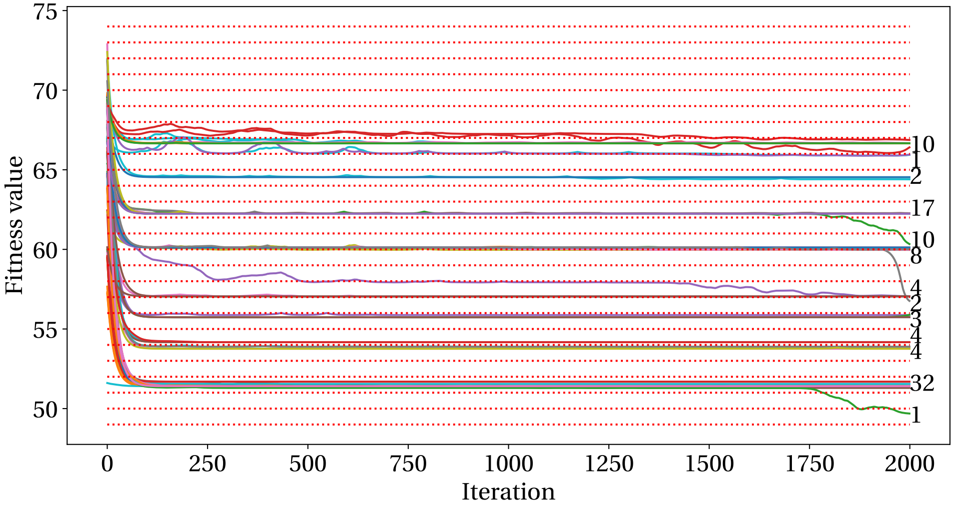

Figure 4.2.: Fitness values of the 98 runs over 2000 iterations. The numbers on the right side of the graph indicate the number of runs that converged in the same region.

Upon examining Figure 4.2, two observations become apparent. Firstly, it is evident that a clear global minimum has not been identified. Despite grouping the final fitness values into regions to mitigate fluctuations introduced by linelength, there are still 13 separate regions where one or more runs converged. This indicates that after 2000 iterations with the current algorithm, no definitive global minimum has been found. Moreover, three runs showed an improvement in fitness within the last 250 iterations, including the overall best run. Further optimization of the algorithm or extending the number of iterations could potentially lead to overall convergence. However, additional iterations require more processing time or power, which was not available for this multistart simulation.

Secondly, it can be observed that after the initial 250 iterations, there is a prolonged period before another decrease in fitness occurs across all runs. This suggests that initially, small adjustments to the initial waveforms facilitate rapid optimization, leading to the discovery of an overall best waveform early on. As this initial optimization phase subsides, all waveforms gradually converge towards the best solution within the population. It appears that during this phase, exploration is insufficient to uncover new and superior waveforms. Towards the end of the iterations, when waveforms converge closer to the overall best, new adjustments to this solution occasionally lead to improved fitness in some cases. This phenomenon is partly inherent to the PSO algorithm's nature, and modifications to enhance exploration could potentially boost performance. Increasing the initial search area would broaden the exploration of possibilities, facilitating more frequent discovery of superior waveforms. The tuning of these parameters is a time-intensive process, as every run has to finish before the next set of parameters can be adjusted appropriately, for which there was no time.

4.3.2. BEST RESULT

Out of the 98 runs conducted, a single best result emerged. The excitation map, which displays activated fibers in green and non-activated fibers in red within a raster representing the cross-section of the CVN, along with the corresponding stimulation waveform, is illustrated in Figure 4.3.

Analyzing the stimulation waves of the two electrodes and their combined effect reveals that EL_1 is the dominant electrode, consistently showing higher amplitudes throughout the stimulation process. This dominance is evident in the activation map, where activated axons are predominantly located in the top left corner (Figure 4.3a), corresponding to EL_1's location. To investigate the role of EL_2 and confirm whether the activation map results from combined stimulation, activation maps for individual stimulation by EL_1 and EL_2 are shown in Figure 4.6.

These figures illustrate that EL_2 contributes to achieving spatial selectivity. When only EL_1 is stimulated and EL_2 is set to zero, the activated area expands, resulting in a fitness deterioration from 50 to 86 (Figure 4.4a). Conversely, when EL_1 is set to zero and EL_2 is stimulated, the fitness deteriorates from 50 to 122 due to the absence of target activation Figure 4.4b. Both scenarios demonstrate reduced spatial selectivity.

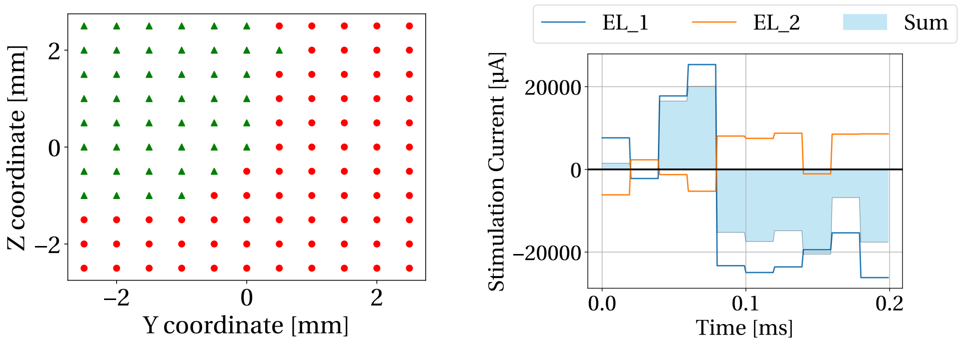

(a) (b)

Figure 4.3.: (a) The excitation map of the best result from the multistart simulation. The green triangles indicate an activated fiber and the red circles are not activated fibers. The fitness value is 50. (b) The stimulation waveform of EL_1 and EL_2. The sum of EL_1 and EL_2 is also depicted as the light blue area.

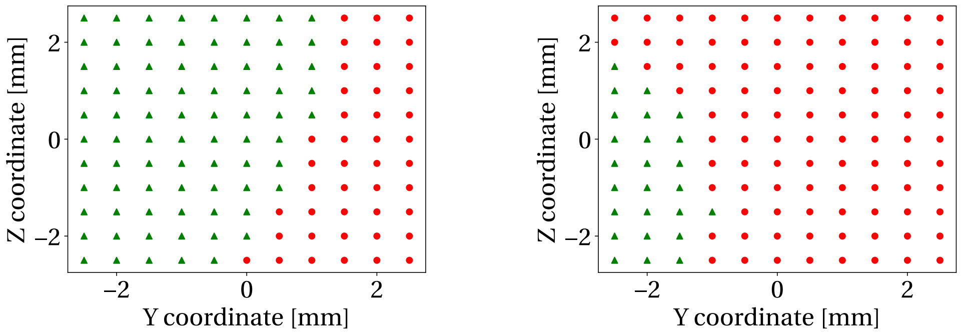

(a) (b)

Figure 4.4.: (a) Excitation map when only the stimulation waveform of EL_1 is present and EL_2 is set to zero, fitness is 86. (b) Excitation map when only the stimulation waveform of EL_2 is present and EL_1 is set to zero. The fitness is 122

Another possible explanation for the spatial selectivity could be the waveform created by the sum of the two electrodes. If stimulating with this summed waveform on a singular electrode still results in the same spatial selectivity, it would suggest that the waveform of the combined electrodes is responsible. To test this hypothesis, the summed waveform depicted in Figure 4.3 was applied individually to electrodes located at EL_1 (Figure 4.5a), EL_2 (Figure 4.5c), and at the coordinate Z = 0mm, y = -5.5mm (Figure 4.5b).

In all three activation maps, the fitness deteriorated compared to the original best result. This indicates that the spatial selectivity achieved by the best result cannot be solely attributed to the waveform resulting from the summed stimulation of EL_1 and EL_2 alone.

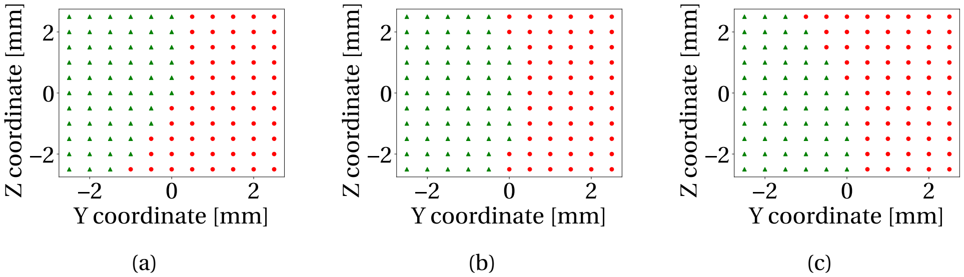

Figure 4.5.: The sum of the waveforms from EL_1 and EL_2 set on a singular electrode on the location of EL_1, fitness = 73 (a), location z = 0mm and y = -5.5mm, fitness = 76 (b) and EL_2, fitness = 73 (c). For all three variations the fitness value worsened

Examining the signal, the spatial selectivity could also be attributed to the fact that the mean amplitude of the waveform of EL_1 is cathodic while that of EL_2 is anodal and that these partly cancel each other out. To test this, the cathodic threshold current for stimulation with only EL_1 was determined, see Figure 4.6a. Then, the anodal current on EL_2 was incrementally increased just before the target was no longer stimulated. This resulted in the activation map Figure 4.6b and a fitness of 72, which is worse than the best result from the multistart simulation. Therefore anodal compensation of cathodic stimulation alone can not explain the best solution found by the multistart simulation.

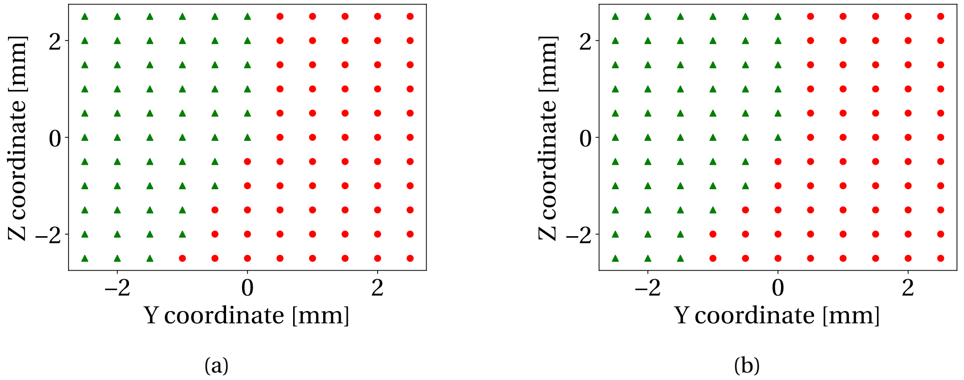

Figure 4.6.: a) Excitation map with only cathodal threshold stimulation on EL_1. b) Excitation map showing anodal compensation by EL_2

To conclude, the observed spatial selectivity cannot be solely attributed to the stimulation of either EL_1 or EL_2 individually. Furthermore, it cannot be explained solely by the waveform created by summing the outputs of both electrodes. Finally, it can also not be attributed to cancellation generated by a stimulation current with opposite polarity. Instead, the selectivity appears to result from the temporal changes in the amplitudes of both EL_1 and EL_2, combined with their specific spatial locations. This interaction creates a temporally and spatially dependent electric field, which is fundamental to TCS.

4.3.3. WAVEFORM IDENTIFICATION

Given that the waveforms are initially generated randomly and then optimized by an algorithm, the resulting output waveforms are not constrained to any specific shape. In this section, we observe different metrics of the resulting waveforms to see if favorable patterns can be identified. Figure 4.7 illustrates the mean of the sum of the two waveforms, as calculated with (4.1). Interestingly, waveforms with a fitness lower than 56 tend to exhibit a negative bias, suggesting that mean cathodic stimulation may lead to better performance. This is further supported by Figure 4.8 that shows that for a fitness lower than 56 the electrode with the highest mean amplitude is cathodic. More interesting in this plot is the fact that the two individual waveforms are always opposite of each other, which suggests some form of cancellation is happening to increase spatial selectivity. Figure 4.7 also indicates asymmetry with respect to the x-axis (for every $f(x,a)$ there is a point $f(x,-a)$). If the waveforms were symmetric, their sum would be zero meaning the two electrode waveforms cancel each other out, which is not observed in the data. Similarly, symmetry over the y-axis does not show a consistent pattern with the performance of different runs (Appendix A). These findings suggest that both the mean waveform characteristics and their asymmetry contribute to the effectiveness of the stimulation, with cathodic dominance playing a large role in achieving lower fitness values.

$$\text{Mean amplitude} = \frac{1}{m}\sum_{n=0}^{m}(\text{EL\_1}_n + \text{EL\_2}_n) \tag{4.1}$$

Where:

m = Number of amplitude changes

EL_1_n = The amplitude of EL_1 at point n

EL_2_n = The amplitude of EL_2 at point n

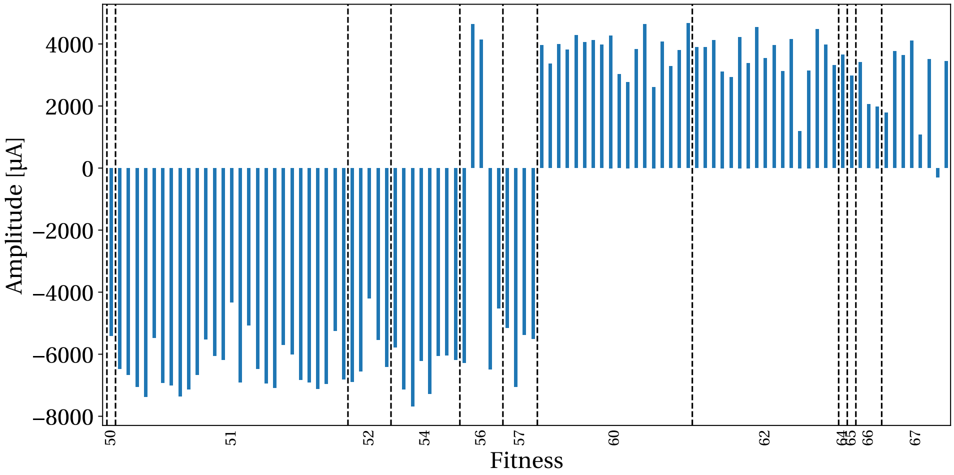

Figure 4.7.: Mean of the sum of the amplitudes from the waveform of EL_1 and EL_2 ordered by their fitness value.

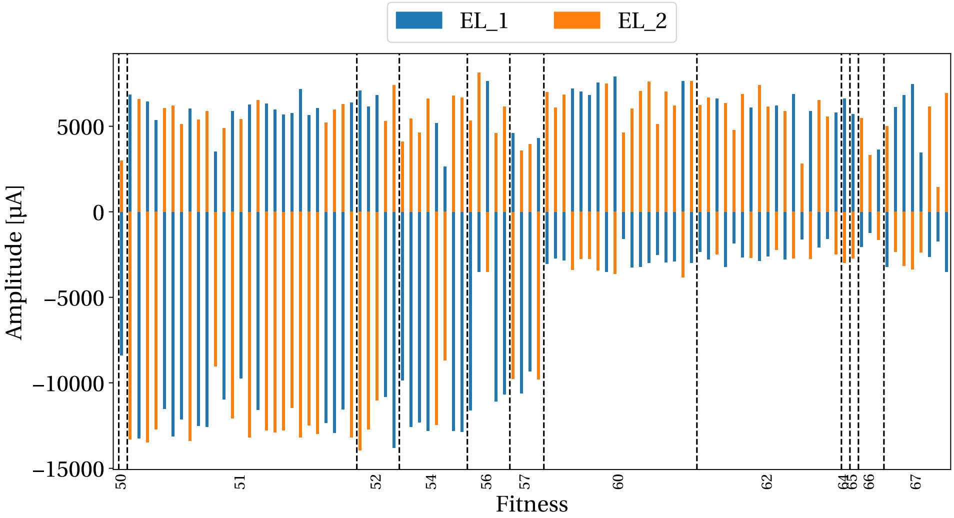

Figure 4.8.: Mean of the waveform amplitude from EL_1 and EL_2 ordered by their fitness value.

Further analysis was conducted on the amount of time waveforms crossed the x-axis or intersected each other to determine if shifts in the signal relate to better fitness values. However, no clear pattern between fitness value and signal crossing was observed (Appendix A).

Additionally, linelength, as depicted in Figure 4.9, which aims to promote signals with fewer fluctuations, does not demonstrate any clear correlation either. These findings suggest that there is no apparent preference for a specific pulse shape or pattern that consistently leads to improved fitness values for the results found with this multistart simulation.

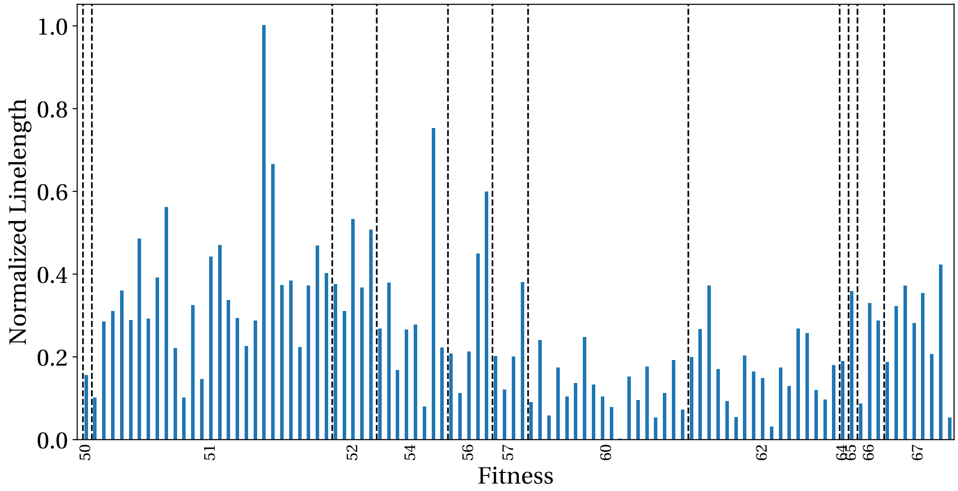

Figure 4.9.: Line length of the waveform per electrode per run normalized .

4.4. TEMPORAL CURRENT STEERING VS DIRECT CURRENT STEERING

To compare TCS with traditional Direct Current Steering (DCS), the simulation environment originally used for TCS was also employed to generate results for DCS. Tests were conducted to assess whether TCS achieves higher spatial selectivity or reduces stimulation charge compared to DCS.

In the DCS simulations, parameters mimicking those used in TCS were applied. A constant direct current of 0.2 ms duration was delivered through two electrodes positioned at EL_1 and EL_2 (Figure 3.2). The threshold currents (I_{th}) for activation were determined under these conditions. Subsequently, simulations were performed where the amplitudes were set as a percentage of $2 * I_{th}$, as depicted in Table 4.2. This way, setting both electrodes to stimulate at 50% resulted in an amplitude of $0.5 * 2 * I_{th} = I_{th}$.

All multistart results of TCS consistently outperformed DCS configurations, which had fitness scores of 73 or higher compared to TCS where the highest fitness was 67. The spatial selectivity generated by DCS configurations 1 and 6 can be observed in Figure 4.10 relative to the overall best TCS result.

Table 4.2.: Simulations executed. The amplitude of the stimulation is 2*I_{th}*Percentage

Nr.	EL_1 %	EL_2 %	Fitness
1	100	0	73
2	90	10	73
3	80	20	74
4	70	30	74
5	60	40	73
6	50	50	75
7	40	60	73
8	30	70	74
9	20	80	74
10	10	90	73
11	0	100	73

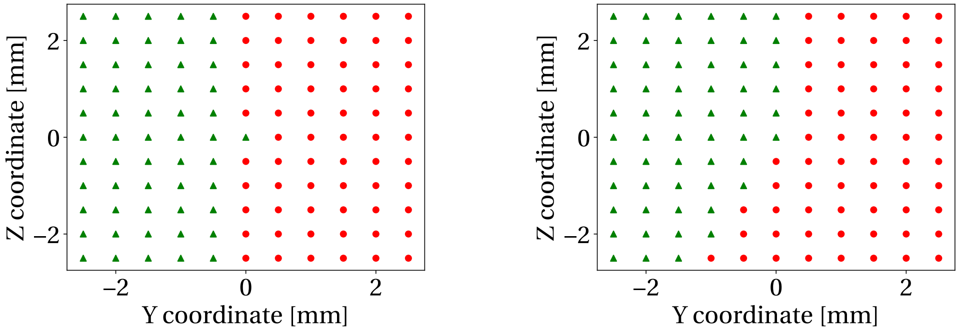

(a)

(b)

Figure 4.10.: Comparison of excitation maps: (a) DCS with Th on both electrodes, (b) DCS with 2*Th on EL_1 and 0 on EL_2.

A similar comparison was conducted for single electrode stimulation, where one electrode was positioned at (10, -5.5, 0) directly in line with the target point, and another at location EL_1. The results depicted in Figure 4.11 show a fitness score of 73 for the single electrode at EL_1 and a fitness score of 72 for the electrode at z = 0mm. These findings indicate that TCS achieves superior spatial selectivity compared to stimulation with a single electrode alone.

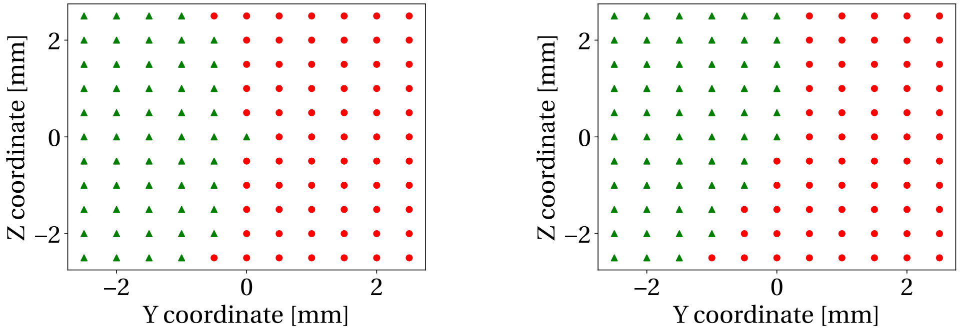

(a)

(b)

Figure 4.11.: A) Excitation map for with a single electrode at z = 0 mm stimulated with threshold current for 0.2ms. B) Excitation map with a single electrode at EL_1 stimulated with threshold current.

Figure 4.12 illustrates fitness values on the x-axis, ordered from best to worst, with stimulation charge plotted on the y-axis. The charge was computed as the maximum current required per timestep multiplied by the timestep (4.2).

While TCS outperforms both DCS and single electrode stimulation in terms of spatial selectivity, it requires more stimulation charge to do so. This increased charge requirement in TCS can potentially be attributed to its cancellation behavior, discussed in subsection 4.3.2, which necessitates additional charge to compensate for the stimulating electrode's effect. The best TCS result with a fitness of 50 requires a 175% increase in charge compared to single electrode stimulation at 0mm, which had a fitness of 72. However, the TCS configuration requiring the least charge still achieves a better fitness of 66 with only a 28% increase in charge compared to the single electrode.

$$\text{Charge} = \sum_{n=0}^{m} (max(|\text{EL\_1}_n|, |\text{EL\_2}_n|) * dt) \tag{4.2}$$

Where:

m = Number of amplitude changes

EL_1_n = The amplitude of EL_1 at point n

EL_2_n = The amplitude of EL_2 at point n

$$dt = \frac{\text{Stimulation time}}{\text{Number of amplitude changes}}$$

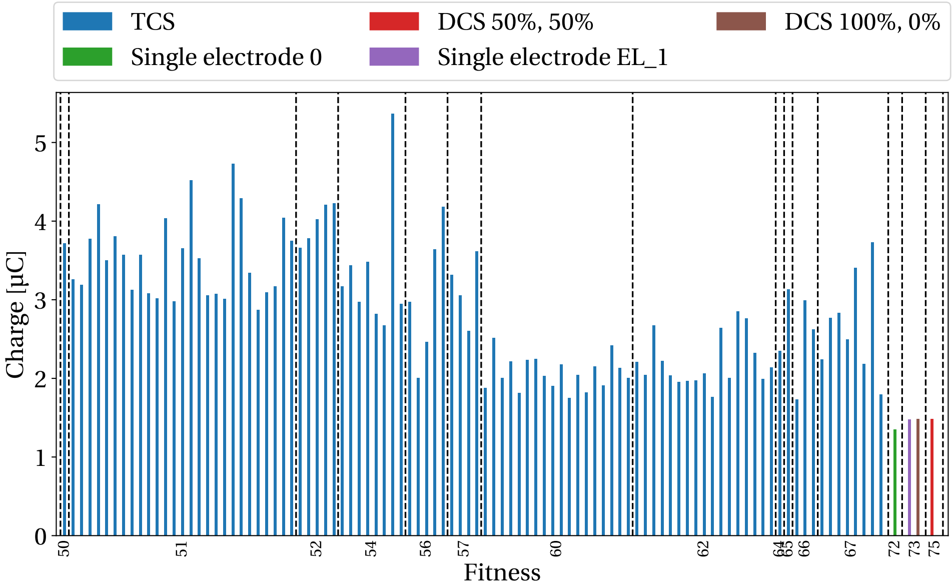

Figure 4.12.: Comparison of stimulation charge between TCS, DCS, and single electrode stimulation ordered by fitness value.

5

DISCUSSION AND CONCLUSION

5.1. DISCUSSION

The primary objective of this thesis was to explore non-invasive stimulation techniques to enhance spatial selectivity for cervical vagus nerve stimulation (CVNS). A novel technique, Temporal Current Steering (TCS), was introduced. TCS splits the stimulation pulse across multiple electrodes, creating a temporal and spatial pattern in the electric field (E-field), hypothesized to increase spatial selectivity within the CVN.

To validate this hypothesis, simulations using NEURON were developed to model the electrodes and their effects on nerve fibers. The simulation can manage up to six electrode locations along with their respective waveforms, generating an activation map that illustrates which nerve fibers are activated in an area representing the cross-section of the cervical vagus nerve. This code was integrated into two optimization algorithms, the genetic algorithm and particle swarm optimization (PSO). After preliminary testing, PSO was selected to run the simulation 98 times with 2000 iterations to identify an optimal waveform. Although convergence on an optimal waveform was not achieved, a single best waveform combination was identified. This optimal solution achieved a 30% improvement over a single electrode placed directly in line with the target and a 31% improvement over the standard current steering technique simulated in the same model. The increased spatial selectivity required a 175% increase in stimulation charge. However, across all runs, the waveform combination that required the least stimulation charge still outperformed the single electrode, achieving a fitness score of 66 with only a 28% increase in stimulation charge.

The original concept of TCS, as discussed in the literature review, was to split a rectangular wave over multiple electrodes, creating a spatially and temporally dependent electric field. However, the optimization algorithm and multistart stimulation used here did not result in simple waveforms like those originally envisioned. Despite this, the waveform resulting from the optimization algorithm still utilizes a spatially and temporally dependent electric field, as shown in subsection 4.3.2. Therefore, the hypothesis of the original concept is indeed validated.

For non-invasive CVNS, additional simulations are needed to validate whether TCS remains effective at a distance of 36 mm between the electrodes on the skin surface and the vagus nerve. These simulations were not performed due to the increase in simulation resources it requires that were not available at this time.

TCS shows great promise for non-invasive CVNS. It outperforms Direct Current Steering (DCS) both in strategically placed single electrodes and in configurations using two electrodes with DCS. The main drawback is the increased stimulation charge, which is noteworthy for invasive stimulation due to faster battery depletion. The charge requirements could potentially be reduced by exploiting the fact that the means of the two waveforms were always opposite in polarity. However, as described in [88], more complex but energy-efficient waveforms do not always result in an overall more energy-efficient system.

5.1.1. RECOMMENDATIONS FOR FUTURE WORK

MODEL

The models used for these simulations were idealized and simplified. Due to restricted computational power, the electrodes were placed at distances that do not resemble those used in non-invasive stimulation. To definitively determine if TCS is viable for non-invasive CVNS, simulations should be run with distances resembling those of the GammaCore device, which has an electrode spacing of 40 mm and a distance to the vagus nerve (VN) of 12.5 mm [7]. This approach would also allow for a good comparison of charge density relative to the GammaCore, where high charge density is a primary cause of the main side effect, skin irritation [60]. Even if TCS does not increase spatial selectivity, it might reduce the charge density, offering a potential benefit.

For non-invasive stimulation, the model should be updated to include a more realistic representation of the VN and the surrounding tissue. If the current model is used, the first improvement could be making the extracellular conductivity anisotropic. Furthermore, for invasive stimulation, the electrode placement should not be limited to a single plane. Greater spatial selectivity could potentially be achieved by arranging the electrodes in a circular pattern around the nerve.

ALGORITHMS

Parameter optimization, of the optimization algorithms was limited due to the necessity of custom implementation of the NEURON software within the optimization code to calculate the fitness value, preventing the use of standard optimization libraries. Future work should focus on optimizing these algorithms by running multiple trial simulations with different parameters to check for convergence, spatial resolution, and waveform shape. Additionally, improvements can be made to the Particle Swarm Optimization (PSO) algorithm by enhancing early exploration during the search process to find better fitness values sooner.

The results shown in Figure 4.2 indicate that there is no certainty that the global minimum has been reached, suggesting that greater spatial selectivity may still be possible.

FITNESS AND RASTER

In addition to tuning the algorithms themselves, refining the fitness function and the activation raster can also increase spatial selectivity. The choice of the target location influences the algorithm's outcome, and this can be leveraged to adjust the location of selectivity. Furthermore, the resolution of the raster can promote different activation map shapes, as the fitness value is a function of the radius of the activated points. A higher resolution can alter this radius in different directions, promoting or demoting certain shapes early on. The overall raster size also plays a crucial role; if the raster is enlarged, additional activations might be detected outside the initial boundaries.

This is particularly important when considering the use of TCS for other applications. For CVN stimulation, only the radius of the VN is important. However, for applications such as deep brain stimulation, where nerves are present 360 degrees around the electrode, the entire surrounding area must be considered. Ensuring that the activation raster accounts for the complete range of potential activations is essential for accurately assessing the efficacy of TCS in these contexts.

5.2. CONCLUSION

Side effects from stimulating the cervical vagus nerve can be reduced by stimulating in a spatially selective manner. However, conventional stimulation devices take the approach of stimulating the whole nerve. In the field of non-invasive electrical neurostimulation, specific waveforms are used to increase spatial selectivity. The goal of this thesis was to explore current non-invasive stimulation techniques to enhance spatial selectivity for cervical vagus nerve stimulation (CVNS). This was achieved by conceptualizing a novel stimulation technique called Temporal Current Steering (TCS), which utilizes a temporally and spatially dependent electric field to increase spatial selectivity.

To validate the feasibility of TCS, a simulation environment was developed where six electrodes can be placed in space with a corresponding amplitude vector to simulate the influence of extracellular stimulation of neurons. The output is an activation raster that displays the activated fibers within the cross-sectional area of the vagus nerve. This setup can be executed with a single command line. Additionally, two optimization algorithms were written in Python, capable of utilizing the simulation code to search for the optimal waveforms using TCS.

Simulation results indicate that TCS is indeed capable of enhancing spatial selectivity within the cervical vagus nerve and performs better than simulated direct current stimulation and optimally placed single electrodes by 30%. The TCS method does not limit itself to only stimulation of the cervical vagus nerve, and implementation with more electrodes could increase spatial selectivity even further. To conclude, TCS is capable of enhancing spatial selectivity for cervical vagus nerve stimulation based on simulation results and should be investigated further to understand its full capabilities.

BIBLIOGRAPHY

[1] J. P. Beekwilder and T. Beems. “Overview of the Clinical Applications of Vagus Nerve Stimulation”. In: *Journal of Clinical Neurophysiology* 27.2 (Apr. 2010), pp. 130–138. ISSN: 0736-0258. DOI: `10.1097/WNP.0b013e3181d64d8a`.

[2] J. W. Wheless, A. J. Gienapp, and P. Ryvlin. “Vagus nerve stimulation (VNS) therapy update”. In: *Epilepsy & Behavior* 88 (Nov. 2018), pp. 2–10. ISSN: 15255050. DOI: `10.1016/j.yebeh.2018.06.032`.

[3] C. Tassorelli, L. Grazzi, M. de Tommaso, G. Pierangeli, P. Martelletti, I. Rainero, S. Dorlas, P. Geppetti, A. Ambrosini, P. Sarchielli, E. Liebler, P. Barbanti, C. Tassorelli, V. Bitetto, R. De Icco, D. Martinelli, G. Sances, M. Bianchi, L. Grazzi, A. M. Padovan, M. de Tommaso, K. Ricci, E. Vecchio, P. Cortelli, S. Cevoli, G. Pierangeli, R. Terlizzi, P. Martelletti, A. Negro, G. A. Chiariello, I. Rainero, P. De Martino, A. Gai, F. Govone, F. Masuzzo, E. Rubino, M. C. Torrieri, A. Vacca, P. Geppetti, A. Chiarugi, F. De Cesaris, S. L. Puma, C. Lupi, I. Marone, A. Ambrosini, A. Perrotta, P. Sarchielli, L. Bernetti, I. Corbelli, M. Romoli, S. Simoni, A. Verzina, P. Barbanti, C. Aurilia, G. Egeo, L. Fofi, E. Liebler, A. Andersson, L. Spitzer, J. Marin, C. McClure, L. Thackerey, M. G. Baldi, and D. Di Maro. “Noninvasive vagus nerve stimulation as acute therapy for migraine”. In: *Neurology* 91.4 (July 2018). ISSN: 0028-3878. DOI: `10.1212/WNL.0000000000005857`. URL: `https://www.neurology.org/doi/10.1212/WNL.0000000000005857`.

[4] A. Fitchett, S. Mastitskaya, and K. Aristovich. “Selective Neuromodulation of the Vagus Nerve”. In: *Frontiers in Neuroscience* 15 (May 2021). ISSN: 1662-453X. DOI: `10.3389/fnins.2021.685872`.

[5] D. T. T. Plachta, M. Gierthmuehlen, O. Cota, N. Espinosa, F. Boeser, T. C. Herrera, T. Stieglitz, and J. Zentner. “Blood pressure control with selective vagal nerve stimulation and minimal side effects”. In: *Journal of Neural Engineering* 11.3 (June 2014), p. 036011. ISSN: 1741-2560. DOI: `10.1088/1741-2560/11/3/036011`.

[6] K. Aristovich, M. Donega, C. Fjordbakk, I. Tarotin, C. A. Chapman, J. Viscasillas, T.-R. Stathopoulou, A. Crawford, D. Chew, J. Perkins, and D. Holder. “Model-based geometrical optimisation and in vivo validation of a spatially selective multielectrode cuff array for vagus nerve neuromodulation”. In: *Journal of Neuroscience Methods* 352 (Mar. 2021), p. 109079. ISSN: 01650270. DOI: `10.1016/j.jneumeth.2021.109079`.

[7] A. P. Mourdoukoutas, D. Q. Truong, D. K. Adair, B. J. Simon, and M. Bikson. “High-Resolution Multi-Scale Computational Model for Non-Invasive Cervical Vagus Nerve Stimulation”. In: *Neuromodulation: Technology at the Neural Interface* 21.3 (Apr. 2018), pp. 261–268. ISSN: 10947159. DOI: `10.1111/ner.12706`. URL: `https://linkinghub.elsevier.com/retrieve/pii/S1094715921022108`.

[8] J. Scherrmann, C. Hoppe, T. Kral, J. Schramm, and C. E. Elger. “Vagus Nerve Stimulation”. In: *Journal of Clinical Neurophysiology* 18.5 (Sept. 2001), pp. 408–414. ISSN: 0736-0258. DOI: `10.1097/00004691-200109000-00004`.

[9] A. Mertens, R. Raedt, S. Gadeyne, E. Carrette, P. Boon, and K. Vonck. “Recent advances in devices for vagus nerve stimulation”. In: *Expert Review of Medical Devices* 15.8 (Aug. 2018), pp. 527–539. ISSN: 1743-4440. DOI: `10.1080/17434440.2018.1507732`.

[10] N. Thompson, S. Mastitskaya, and D. Holder. “Avoiding off-target effects in electrical stimulation of the cervical vagus nerve: Neuroanatomical tracing techniques to study fascicular anatomy of the vagus nerve”. In: *Journal of Neuroscience Methods* 325 (Sept. 2019), p. 108325. ISSN: 01650270. DOI: `10.1016/j.jneumeth.2019.108325`.

[11] M. Dali, O. Rossel, D. Andreu, L. Laporte, A. Hernández, J. Laforet, E. Marijon, A. Hagège, M. Clerc, C. Henry, and D. Guiraud. “Model based optimal multipolar stimulation without <i>a priori</i> knowledge of nerve structure: application to vagus nerve stimulation”. In: *Journal of Neural Engineering* 15.4 (Aug. 2018), p. 046018. ISSN: 1741-2560. DOI: `10.1088/1741-2552/aabeb9`.

[12] E. N. Marieb and K. Hoehn. *Human Anatomy & Physiology*. Eleventh. Pearson Education Limited, 2019, pp. 569–569.

[13] S. L. Helmers, J. Begnaud, A. Cowley, H. M. Corwin, J. C. Edwards, D. L. Holder, H. Kostov, P. G. Larsson, P. M. Levisohn, M. S. Menezes, H. Stefan, and D. M. Labiner. “Application of a computational model of vagus nerve stimulation”. In: *Acta Neurologica Scandinavica* 126.5 (Nov. 2012), pp. 336–343. ISSN: 0001-6314. DOI: `10.1111/j.1600-0404.2012.01656.x`.

[14] R. Carron, P. Roncon, S. Lagarde, M. Dibué, M. Zanello, and F. Bartolomei. “Latest Views on the Mechanisms of Action of Surgically Implanted Cervical Vagal Nerve Stimulation in Epilepsy”. In: *Neuromodulation: Technology at the Neural Interface* 26.3 (Apr. 2023), pp. 498–506. ISSN: 10947159. DOI: `10.1016/j.neurom.2022.08.447`.

[15] N. Jayaprakash, W. Song, V. Toth, A. Vardhan, T. Levy, J. Tomaio, K. Qanud, I. Mughrabi, Y.-C. Chang, M. Rob, A. Daytz, A. Abbas, Z. Nassrallah, B. T. Volpe, K. J. Tracey, Y. Al-Abed, T. Datta-Chaudhuri, L. Miller, M. F. Barbe, S. C. Lee, T. P. Zanos, and S. Zanos. “Organ- and function-specific anatomical organization of vagal fibers supports fascicular vagus nerve stimulation”. In: *Brain Stimulation* 16.2 (Mar. 2023), pp. 484–506. ISSN: 1935861X. DOI: `10.1016/j.brs.2023.02.003`.

[16] K. Shin, Y. M. Bae, H.-S. Park, D.-G. Kang, and M. Kang. "The Effect of Electrode Distance on the Voltage Distribution during Non-invasive Vagus Nerve Stimulation – a Preliminary Study". In: *2023 International Conference on Electronics, Information, and Communication (ICEIC)*. IEEE, Feb. 2023, pp. 1–3. ISBN: 979-8-3503-2021-3. DOI: 10.1109/ICEIC57457.2023.10049951. URL: https://ieeexplore.ieee.org/document/10049951/.

[17] N. Hammer, S. Löffler, Y. O. Cakmak, B. Ondruschka, U. Planitzer, M. Schultz, D. Winkler, and D. Weise. "Cervical vagus nerve morphometry and vascularity in the context of nerve stimulation - A cadaveric study". In: *Scientific Reports* 8.1 (May 2018), p. 7997. ISSN: 2045-2322. DOI: 10.1038/s41598-018-26135-8.

[18] J. Malmivuo and R. Plonsey. *BioelectromagnetismPrinciples and Applications of Bioelectric and Biomagnetic Fields*. Oxford University Press, Oct. 1995. ISBN: 9780195058239. DOI: 10.1093/acprof:oso/9780195058239.001.0001. URL: https://academic.oup.com/book/25966.

[19] A. L. Hodgkin and A. F. Huxley. "A quantitative description of membrane current and its application to conduction and excitation in nerve". In: *The Journal of Physiology* 117.4 (Aug. 1952), pp. 500–544. ISSN: 0022-3751. DOI: 10.1113/jphysiol.1952.sp004764.

[20] J. P. Reilly and A. M. Diamant. *Electrostimulation : Theory, Applications, and Computational Model*. Norwood, UNITED STATES: Artech House, 2011. ISBN: 9781608071098. URL: http://ebookcentral.proquest.com/lib/delft/detail.action?docID=717879.

[21] Liu Shi Gan and A. Prochazka. "Properties of the Stimulus Router System, a Novel Neural Prosthesis". In: *IEEE Transactions on Biomedical Engineering* 57.2 (Feb. 2010), pp. 450–459. ISSN: 0018-9294. DOI: 10.1109/TBME.2009.2031427.

[22] H. Bostock. "The strength-duration relationship for excitation of myelinated nerve: computed dependence on membrane parameters." In: *The Journal of Physiology* 341.1 (Aug. 1983), pp. 59–74. ISSN: 00223751. DOI: 10.1113/jphysiol.1983.sp014792. URL: https://onlinelibrary.wiley.com/doi/10.1113/jphysiol.1983.sp014792.

[23] N. Grossman, D. Bono, N. Dedic, S. B. Kodandaramaiah, A. Rudenko, H.-J. Suk, A. M. Cassara, E. Neufeld, N. Kuster, L.-H. Tsai, A. Pascual-Leone, and E. S. Boyden. "Noninvasive Deep Brain Stimulation via Temporally Interfering Electric Fields". In: *Cell* 169.6 (June 2017), pp. 1029–1041. ISSN: 00928674. DOI: 10.1016/j.cell.2017.05.024. URL: https://linkinghub.elsevier.com/retrieve/pii/S0092867417305846.

[24] A. G. Pakhomov, I. Semenov, S. Xiao, O. N. Pakhomova, B. Gregory, K. H. Schoenbach, J. C. Ullery, H. T. Beier, S. R. Rajulapati, and B. L. Ibey. "Cancellation of cellular responses to nanoelectroporation by reversing the stimulus polarity". In: *Cellular and Molecular Life Sciences* 71.22 (Nov. 2014), pp. 4431–4441. ISSN: 14209071. DOI: 10.1007/s00018-014-1626-z.

[25] A. Kuhn and T. Keller. “A selectivity measure for transcutaneous electrodes”. In: *International Functional Electrical Stimulation Society Conference, Philadelphia, PA*. 2007.

[26] T. Keller and A. Kuhn. “Electrodes for transcutaneous (surface) electrical stimulation”. In: *Journal of Automatic Control* 18.2 (2008), pp. 35–45. ISSN: 1450-9903. DOI: 10.2298/JAC0802035K.

[27] I. Jones and M. I. Johnson. “Transcutaneous electrical nerve stimulation”. In: *Continuing Education in Anaesthesia Critical Care & Pain* 9.4 (Aug. 2009), pp. 130–135. ISSN: 17431816. DOI: 10.1093/bjaceaccp/mkp021.

[28] A. Kuhn, T. Keller, M. Lawrence, and M. Morari. “A model for transcutaneous current stimulation: simulations and experiments”. In: *Medical & Biological Engineering & Computing* 47.3 (Mar. 2009), pp. 279–289. ISSN: 0140-0118. DOI: 10.1007/s11517-008-0422-z.

[29] F. Fregni, L. Grecco, S. Li, S. Michel, L. Castillo-Saavedra, A. Mourdoukoutas, and M. Bikson. “Transcutaneous spinal stimulation as a therapeutic strategy for spinal cord injury: state of the art”. In: *Journal of Neurorestoratology* (Mar. 2015), p. 73. ISSN: 2324-2426. DOI: 10.2147/JN.S77813.

[30] J. Redgrave, D. Day, H. Leung, P. Laud, A. Ali, R. Lindert, and A. Majid. “Safety and tolerability of Transcutaneous Vagus Nerve stimulation in humans; a systematic review”. In: *Brain Stimulation* 11.6 (Nov. 2018), pp. 1225–1238. ISSN: 1935861X. DOI: 10.1016/j.brs.2018.08.010.

[31] M. I. Johnson, C. H. Ashton, and J. W. Thompson. “An in-depth study of long-term users of transcutaneous electrical nerve stimulation (TENS). Implications for clinical use of TENS”. In: *Pain* 44.3 (Mar. 1991), pp. 221–229. ISSN: 0304-3959. DOI: 10.1016/0304-3959(91)90089-G.

[32] A. Barikroo, G. Carnaby, D. Bolser, R. Rozensky, and M. Crary. “Transcutaneous electrical stimulation on the anterior neck region: The impact of pulse duration and frequency on maximum amplitude tolerance and perceived discomfort”. In: *Journal of Oral Rehabilitation* 45.6 (June 2018), pp. 436–441. ISSN: 0305-182X. DOI: 10.1111/joor.12625. URL: https://onlinelibrary.wiley.com/doi/10.1111/joor.12625.

[33] A. Kuhn, T. Keller, S. Micera, and M. Morari. “Array electrode design for transcutaneous electrical stimulation: A simulation study”. In: *Medical Engineering & Physics* 31.8 (Oct. 2009), pp. 945–951. ISSN: 13504533. DOI: 10.1016/j.medengphy.2009.05.006.

[34] T. Keller, M. Lawrence, A. Kuhn, and M. Morari. “New Multi-Channel Transcutaneous Electrical Stimulation Technology for Rehabilitation”. In: *2006 International Conference of the IEEE Engineering in Medicine and Biology Society*. IEEE, Aug. 2006, pp. 194–197. ISBN: 1-4244-0032-5. DOI: 10.1109/IEMBS.2006.259399.

[35] A. Popović-Bijelić, G. Bijelić, N. Jorgovanović, D. Bojanić, M. B. Popović, and D. B. Popović. "Multi-Field Surface Electrode for Selective Electrical Stimulation". In: *Artificial Organs* 29.6 (June 2005), pp. 448–452. ISSN: 0160-564X. DOI: `10.1111/j.1525-1594.2005.29075.x`.

[36] L. E. Medina and W. M. Grill. "Volume conductor model of transcutaneous electrical stimulation with kilohertz signals". In: *Journal of Neural Engineering* 11.6 (Dec. 2014), p. 066012. ISSN: 1741-2560. DOI: `10.1088/1741-2560/11/6/066012`.

[37] E. Mirzakhalili, B. Barra, M. Capogrosso, and S. F. Lempka. "Biophysics of Temporal Interference Stimulation". In: *Cell Systems* 11.6 (Dec. 2020), pp. 557–572. ISSN: 24054712. DOI: `10.1016/j.cels.2020.10.004`. URL: `https://linkinghub.elsevier.com/retrieve/pii/S2405471220303720`.

[38] R. B. Budde, M. T. Williams, and P. P. Irazoqui. "Temporal interference current stimulation in peripheral nerves is not driven by envelope extraction". In: *Journal of Neural Engineering* 20.2 (Apr. 2023), p. 026041. ISSN: 1741-2560. DOI: `10.1088/1741-2552/acc6f1`. URL: `https://iopscience.iop.org/article/10.1088/1741-2552/acc6f1`.

[39] K. H. Schoenbach, B. Hargrave, R. P. Joshi, J. F. Kolb, R. Nuccitelli, C. Osgood, A. Pakhomov, M. Stacey, R. J. Swanson, J. A. White, S. Xiao, J. Zhang, S. J. Beebe, P. F. Blackmore, and E. Stephen Buescher. *Bioelectric Effects of Intense Nanosecond Pulses*. Tech. rep. 2007. DOI: `10.1109/TDEI.2007.4339468`.

[40] J. Gehl. *Electroporation: Theory and methods, perspectives for drug delivery, gene therapy and research*. Apr. 2003. DOI: `10.1046/j.1365-201X.2003.01093.x`.

[41] K. Kinosita and T. Y. Tsong. "Voltage-induced pore formation and hemolysis of human erythrocytes". In: *Biochimica et Biophysica Acta (BBA) - Biomembranes* 471.2 (Dec. 1977), pp. 227–242. ISSN: 00052736. DOI: `10.1016/0005-2736(77)90252-8`.

[42] J. Teissié and M. Rols. "An experimental evaluation of the critical potential difference inducing cell membrane electropermeabilization". In: *Biophysical Journal* 65.1 (July 1993), pp. 409–413. ISSN: 00063495. DOI: `10.1016/S0006-3495(93)81052-X`.

[43] K. H. Schoenbach, S. J. Beebe, and E. S. Buescher. "Intracellular effect of ultrashort electrical pulses". In: *Bioelectromagnetics* 22.6 (Sept. 2001), pp. 440–448. ISSN: 01978462. DOI: `10.1002/bem.71`.

[44] S. J. Beebe, P. M. Fox, L. J. Rec, L. K. Willis, and K. H. Schoenbach. "Nanosecond, high-intensity pulsed electric fields induce apoptosis in human cells". In: *The FASEB Journal* 17.11 (Aug. 2003), pp. 1–23. ISSN: 0892-6638. DOI: `10.1096/fj.02-0859fje`.

[45] M. Casciola, S. Xiao, and A. G. Pakhomov. "Damage-free peripheral nerve stimulation by 12-ns pulsed electric field". In: *Scientific Reports* 7.1 (Dec. 2017). ISSN: 20452322. DOI: `10.1038/s41598-017-10282-5`.

[46] P. Lamberti, M. Compitiello, and S. Romeo. “ns Pulsed Electric Field-Induced Action Potentials in the Circuital Model of an Axon”. In: *IEEE Transactions on Nanobioscience* 17.2 (Apr. 2018), pp. 110–116. ISSN: 15361241. DOI: 10.1109/TNB.2018.2822840.

[47] E. C. Gianulis, M. Casciola, C. Zhou, E. Yang, S. Xiao, and A. G. Pakhomov. “Selective distant electrostimulation by synchronized bipolar nanosecond pulses”. In: *Scientific Reports* 9.1 (Sept. 2019), p. 13116. ISSN: 2045-2322. DOI: 10.1038/s41598-019-49664-2. URL: https://www.nature.com/articles/s41598-019-49664-2.

[48] A. G. Pakhomov, E. Gudvangen, S. Xiao, and I. Semenov. “Interference targeting of bipolar nanosecond electric pulses for spatially focused electroporation, electrostimulation, and tissue ablation”. In: *Bioelectrochemistry* 141 (Oct. 2021). ISSN: 1878562X. DOI: 10.1016/j.bioelechem.2021.107876.

[49] A. G. Pakhomov, E. Gudvangen, U. Mangalanathan, O. Kondratiev, L. Redondo, and I. Semenov. “Next generation CANCAN focusing for remote stimulation by nanosecond electric pulses”. In: *Bioelectrochemistry* 152 (Aug. 2023). ISSN: 1878562X. DOI: 10.1016/j.bioelechem.2023.108437.

[50] A. Fertonani and C. Miniussi. “Transcranial Electrical Stimulation”. In: *The Neuroscientist* 23.2 (Apr. 2017), pp. 109–123. ISSN: 1073-8584. DOI: 10.1177/1073858416631966. URL: http://journals.sagepub.com/doi/10.1177/1073858416631966.

[51] W. Paulus. “Transcranial electrical stimulation (tES – tDCS; tRNS, tACS) methods”. In: *Neuropsychological Rehabilitation* 21.5 (Oct. 2011), pp. 602–617. ISSN: 0960-2011. DOI: 10.1080/09602011.2011.557292. URL: http://www.tandfonline.com/doi/abs/10.1080/09602011.2011.557292.

[52] F. Yavari, A. Jamil, M. Mosayebi Samani, L. P. Vidor, and M. A. Nitsche. “Basic and functional effects of transcranial Electrical Stimulation (tES)—An introduction”. In: *Neuroscience & Biobehavioral Reviews* 85 (Feb. 2018), pp. 81–92. ISSN: 01497634. DOI: 10.1016/j.neubiorev.2017.06.015.

[53] A. Datta, V. Bansal, J. Diaz, J. Patel, D. Reato, and M. Bikson. “Gyri-precise head model of transcranial direct current stimulation: Improved spatial focality using a ring electrode versus conventional rectangular pad”. In: *Brain Stimulation* 2.4 (Oct. 2009), pp. 201–207. ISSN: 1935861X. DOI: 10.1016/j.brs.2009.03.005.

[54] S. Ueno and M. Sekino. “Figure-Eight Coils for Magnetic Stimulation: From Focal Stimulation to Deep Stimulation”. In: *Frontiers in Human Neuroscience* 15 (Dec. 2021). ISSN: 1662-5161. DOI: 10.3389/fnhum.2021.805971.

[55] M. Hallett. “Transcranial Magnetic Stimulation: A Primer”. In: *Neuron* 55.2 (July 2007), pp. 187–199. ISSN: 08966273. DOI: 10.1016/j.neuron.2007.06.026.

[56] M. Kobayashi and A. Pascual-Leone. “Transcranial magnetic stimulation in neurology”. In: *The Lancet Neurology* 2.3 (Mar. 2003), pp. 145–156. ISSN: 14744422. DOI: 10.1016/S1474-4422(03)00321-1.

[57] B. Passera, A. Chauvin, E. Raffin, T. Bougerol, O. David, and S. Harquel. “Exploring the spatial resolution of TMS-EEG coupling on the sensorimotor region”. In: *NeuroImage* 259 (Oct. 2022), p. 119419. ISSN: 10538119. DOI: `10.1016/j.neuroimage.2022.119419`. URL: `https://linkinghub.elsevier.com/retrieve/pii/S1053811922005365`.

[58] M. W. Sliwinska, S. Vitello, and J. T. Devlin. “Transcranial Magnetic Stimulation for Investigating Causal Brain-behavioral Relationships and their Time Course”. In: *Journal of Visualized Experiments* 89 (July 2014). ISSN: 1940-087X. DOI: `10.3791/51735`.

[59] A. Pitzus, S. Romeni, F. Vallone, and S. Micera. “A method to establish functional vagus nerve topography from electro-neurographic spontaneous activity”. In: *Patterns* 3.11 (Nov. 2022), p. 100615. ISSN: 26663899. DOI: `10.1016/j.patter.2022.100615`.

[60] E. Ben-Menachem, D. Revesz, B. J. Simon, and S. Silberstein. “Surgically implanted and non-invasive vagus nerve stimulation: a review of efficacy, safety and tolerability”. In: *European Journal of Neurology* 22.9 (Sept. 2015), pp. 1260–1268. ISSN: 1351-5101. DOI: `10.1111/ene.12629`. URL: `https://onlinelibrary.wiley.com/doi/10.1111/ene.12629`.

[61] D. H. Toffa, L. Touma, T. El Meskine, A. Bouthillier, and D. K. Nguyen. “Learnings from 30 years of reported efficacy and safety of vagus nerve stimulation (VNS) for epilepsy treatment: A critical review”. In: *Seizure* 83 (Dec. 2020), pp. 104–123. ISSN: 10591311. DOI: `10.1016/j.seizure.2020.09.027`.

[62] U. C. Schneider, K. Bohlmann, P. Vajkoczy, and H.-B. Straub. “Implantation of a new Vagus Nerve Stimulation (VNS) Therapy® generator, AspireSR®: considerations and recommendations during implantation and replacement surgery—comparison to a traditional system”. In: *Acta Neurochirurgica* 157.4 (Apr. 2015), pp. 721–728. ISSN: 0001-6268. DOI: `10.1007/s00701-015-2362-3`.

[63] H. Yuan and S. D. Silberstein. “Vagus Nerve and Vagus Nerve Stimulation, a Comprehensive Review: Part II”. In: *Headache: The Journal of Head and Face Pain* 56.2 (Feb. 2016), pp. 259–266. ISSN: 0017-8748. DOI: `10.1111/head.12650`.

[64] J. Dawson, D. Pierce, A. Dixit, T. J. Kimberley, M. Robertson, B. Tarver, O. Hilmi, J. McLean, K. Forbes, M. P. Kilgard, R. L. Rennaker, S. C. Cramer, M. Walters, and N. Engineer. “Safety, Feasibility, and Efficacy of Vagus Nerve Stimulation Paired With Upper-Limb Rehabilitation After Ischemic Stroke”. In: *Stroke* 47.1 (Jan. 2016), pp. 143–150. ISSN: 0039-2499. DOI: `10.1161/STROKEAHA.115.010477`.

[65] F. Giordano, A. Zicca, C. Barba, R. Guerrini, and L. Genitori. “Vagus nerve stimulation: Surgical technique of implantation and revision and related morbidity”. In: *Epilepsia* 58.S1 (Apr. 2017), pp. 85–90. ISSN: 0013-9580. DOI: `10.1111/epi.13678`.

[66] S. D. Silberstein, L. L. Mechtler, D. B. Kudrow, A. H. Calhoun, C. McClure, J. R. Saper, E. J. Liebler, E. Rubenstein Engel, and S. J. Tepper. "Non–Invasive Vagus Nerve Stimulation for the ACute Treatment of Cluster Headache: Findings From the Randomized, Double-Blind, Sham-Controlled ACT1 Study". In: *Headache: The Journal of Head and Face Pain* 56.8 (Sept. 2016), pp. 1317–1332. ISSN: 0017-8748. DOI: 10.1111/head.12896.

[67] I. S. Lendvai, A. Maier, D. Scheele, R. Hurlemann, and T. M. Kinfe. "Spotlight on cervical vagus nerve stimulation for the treatment of primary headache disorders: a review". In: *Journal of Pain Research* Volume 11 (Aug. 2018), pp. 1613–1625. ISSN: 1178-7090. DOI: 10.2147/JPR.S129202.

[68] H. Yuan and S. D. Silberstein. "Vagus Nerve and Vagus Nerve Stimulation, a Comprehensive Review: Part III". In: *Headache: The Journal of Head and Face Pain* 56.3 (Mar. 2016), pp. 479–490. ISSN: 0017-8748. DOI: 10.1111/head.12649.

[69] K. Moazzami, B. D. Pearce, N. Z. Gurel, M. T. Wittbrodt, O. M. Levantsevych, M. Huang, M. M. H. Shandhi, I. Herring, N. Murrah, E. Driggers, M. L. Alkhalaf, M. Soudan, L. Shallenberger, A. N. Hankus, J. A. Nye, V. Vaccarino, A. J. Shah, O. T. Inan, and J. D. Bremner. "Transcutaneous vagal nerve stimulation modulates stress-induced plasma ghrelin levels: A double-blind, randomized, sham-controlled trial". In: *Journal of Affective Disorders* 342 (Dec. 2023), pp. 85–90. ISSN: 01650327. DOI: 10.1016/j.jad.2023.09.015.

[70] J. Ellrich. "Transcutaneous Vagus Nerve Stimulation". In: *European Neurological Review* 6.4 (2011), p. 254. ISSN: 1758-3837. DOI: 10.17925/ENR.2011.06.04.254.

[71] S. Nagami, K. Maeda, S. Fukunaga, M. Ikeno, and Y. Oku. "Safety of transcutaneous electrical sensory stimulation of the neck in terms of vital parameters in dysphagia rehabilitation". In: *Scientific Reports* 9.1 (Sept. 2019), p. 13481. ISSN: 2045-2322. DOI: 10.1038/s41598-019-49954-9.

[72] M.-X. Wang, A. Wumiti, Y.-W. Zhang, X.-S. Gao, Z. Huang, M.-F. Zhang, Z.-Y. Peng, Y. Oku, and Z.-M. Tang. "Transcutaneous cervical vagus nerve stimulation improved motor cortex excitability in healthy adults: a randomized, single-blind, self-crossover design study". In: *Frontiers in Neuroscience* 17 (Oct. 2023). ISSN: 1662-453X. DOI: 10.3389/fnins.2023.1234033.

[73] T. Furuta, M. Takemura, J. Tsujita, and Y. Oku. "Interferential Electric Stimulation Applied to the Neck Increases Swallowing Frequency". In: *Dysphagia* 27.1 (Mar. 2012), pp. 94–100. ISSN: 0179-051X. DOI: 10.1007/s00455-011-9344-2.

[74] J. E. Bucksot, A. J. Wells, K. C. Rahebi, V. Sivaji, M. Romero-Ortega, M. P. Kilgard, R. L. Rennaker, and S. A. Hays. "Flat electrode contacts for vagus nerve stimulation". In: *PLOS ONE* 14.11 (Nov. 2019), e0215191. ISSN: 1932-6203. DOI: 10.1371/journal.pone.0215191.

[75] M. Tosato, K. Yoshida, E. Toft, and J. J. Struijk. “Quasi-trapezoidal pulses to selectively block the activation of intrinsic laryngeal muscles during vagal nerve stimulation”. In: *Journal of Neural Engineering* 4.3 (Sept. 2007), pp. 205–212. ISSN: 1741-2560. DOI: 10.1088/1741-2560/4/3/005.

[76] P. Peclin and J. Rozman. “A Model of Selective Left VNS and Recording in a Man”. In: 2009, pp. 147–150. DOI: 10.1007/978-3-642-04292-8{_}33.

[77] K. Y. Qing, M. P. Ward, and P. P. Irazoqui. “Burst-Modulated Waveforms Optimize Electrical Stimuli for Charge Efficiency and Fiber Selectivity”. In: *IEEE Transactions on Neural Systems and Rehabilitation Engineering* 23.6 (Nov. 2015), pp. 936–945. ISSN: 1534-4320. DOI: 10.1109/TNSRE.2015.2421732.

[78] M. Dali, C. Picq, O. Rossel, P. Maciejasz, C.-H. Malbert, and D. Guiraud. “Comparison of the efficiency of chopped and non-rectangular electrical stimulus waveforms in activating small vagus nerve fibers”. In: *Journal of Neuroscience Methods* 320 (May 2019), pp. 1–8. ISSN: 01650270. DOI: 10.1016/j.jneumeth.2019.02.017.

[79] U. Ahmed, Y.-C. Chang, M. Cracchiolo, M. F. Lopez, J. N. Tomaio, T. Datta-Chaudhuri, T. P. Zanos, L. Rieth, Y. Al-Abed, and S. Zanos. “Anodal block permits directional vagus nerve stimulation”. In: *Scientific Reports* 10.1 (June 2020), p. 9221. ISSN: 2045-2322. DOI: 10.1038/s41598-020-66332-y.

[80] S. C. M. A. Ordelman, L. Kornet, R. Cornelussen, H. P. J. Buschman, and P. H. Veltink. “Selectivity for Specific Cardiovascular Effects of Vagal Nerve Stimulation With a Multi-Contact Electrode Cuff”. In: *IEEE Transactions on Neural Systems and Rehabilitation Engineering* 21.1 (Jan. 2013), pp. 32–36. ISSN: 1534-4320. DOI: 10.1109/TNSRE.2012.2214058.

[81] D. T. T. Plachta, M. Gierthmuehlen, O. Cota, F. Boeser, and T. Stieglitz. “BaroLoop: Using a multichannel cuff electrode and selective stimulation to reduce blood pressure”. In: *2013 35th Annual International Conference of the IEEE Engineering in Medicine and Biology Society (EMBC)*. IEEE, July 2013, pp. 755–758. ISBN: 978-1-4577-0216-7. DOI: 10.1109/EMBC.2013.6609610.

[82] E. Ravagli, J. Ardell, D. Holder, and K. Aristovich. “A combined cuff electrode array for organ-specific selective stimulation of vagus nerve enabled by Electrical Impedance Tomography”. In: *Frontiers in Medical Technology* 5 (Apr. 2023). ISSN: 2673-3129. DOI: 10.3389/fmedt.2023.1122016.

[83] C. R. Butson and C. C. McIntyre. “Current steering to control the volume of tissue activated during deep brain stimulation”. In: *Brain Stimulation* 1.1 (Jan. 2008), pp. 7–15. ISSN: 1935861X. DOI: 10.1016/j.brs.2007.08.004.

[84] A. Chaturvedi, T. J. Foutz, and C. C. McIntyre. “Current steering to activate targeted neural pathways during deep brain stimulation of the subthalamic region”. In: *Brain Stimulation* 5.3 (July 2012), pp. 369–377. ISSN: 1935861X. DOI: 10.1016/j.brs.2011.05.002.

[85] T. C. Spencer, J. B. Fallon, and M. N. Shivdasani. “Creating virtual electrodes with 2D current steering”. In: *Journal of Neural Engineering* 15.3 (June 2018), p. 035002. ISSN: 1741-2560. DOI: 10.1088/1741-2552/aab1b8.

[86] Y. A. Patel and R. J. Butera. “Differential fiber-specific block of nerve conduction in mammalian peripheral nerves using kilohertz electrical stimulation”. In: *Journal of Neurophysiology* 113.10 (June 2015), pp. 3923–3929. ISSN: 0022-3077. DOI: `10.1152/jn.00529.2014`.

[87] Y. A. Patel, T. Saxena, R. V. Bellamkonda, and R. J. Butera. “Kilohertz frequency nerve block enhances anti-inflammatory effects of vagus nerve stimulation”. In: *Scientific Reports* 7.1 (Jan. 2017), p. 39810. ISSN: 2045-2322. DOI: `10.1038/srep39810`.

[88] F. Varkevisser, T. L. Costa, and W. A. Serdijn. “Energy efficiency of pulse shaping in electrical stimulation: the interdependence of biophysical effects and circuit design losses”. In: *Biomedical Physics & Engineering Express* 8.6 (Nov. 2022), p. 065009. ISSN: 2057-1976. DOI: `10.1088/2057-1976/ac8c47`.

[89] A. Wongsarnpigoon and W. M. Grill. “Energy-efficient waveform shapes for neural stimulation revealed with a genetic algorithm”. In: *Journal of Neural Engineering* 7.4 (Aug. 2010), p. 046009. ISSN: 1741-2560. DOI: `10.1088/1741-2560/7/4/046009`. URL: `https://iopscience.iop.org/article/10.1088/1741-2560/7/4/046009`.

[90] N. T. Carnevale and M. L. Hines. *The NEURON Book*. Cambridge University Press, Jan. 2006. ISBN: 9780521843218. DOI: `10.1017/CBO9780511541612`.

[91] E. J. Peterson, O. Izad, and D. J. Tyler. “Predicting myelinated axon activation using spatial characteristics of the extracellular field”. In: *Journal of Neural Engineering* 8.4 (Aug. 2011), p. 046030. ISSN: 1741-2560. DOI: `10.1088/1741-2560/8/4/046030`. URL: `https://iopscience.iop.org/article/10.1088/1741-2560/8/4/046030`.

[92] C. C. McIntyre, A. G. Richardson, and W. M. Grill. “Modeling the Excitability of Mammalian Nerve Fibers: Influence of Afterpotentials on the Recovery Cycle”. In: *Journal of Neurophysiology* 87.2 (Feb. 2002), pp. 995–1006. ISSN: 0022-3077. DOI: `10.1152/jn.00353.2001`.

[93] T. J. M. Verlinden, K. Rijkers, G. Hoogland, and A. Herrler. “Morphology of the human cervical vagus nerve: implications for vagus nerve stimulation treatment”. In: *Acta Neurologica Scandinavica* 133.3 (Mar. 2016), pp. 173–182. ISSN: 00016314. DOI: `10.1111/ane.12462`. URL: `https://onlinelibrary.wiley.com/doi/10.1111/ane.12462`.

[94] L. A. Havton, N. P. Biscola, E. Stern, P. V. Mihaylov, C. A. Kubal, J. M. Wo, A. Gupta, E. Baronowsky, M. P. Ward, D. M. Jaffey, and T. L. Powley. “Human organ donor-derived vagus nerve biopsies allow for well-preserved ultrastructure and high-resolution mapping of myelinated and unmyelinated fibers”. In: *Scientific Reports* 11.1 (Dec. 2021), p. 23831. ISSN: 2045-2322. DOI: `10.1038/s41598-021-03248-1`.

[95] E. Warman, W. Grill, and D. Durand. “Modeling the effects of electric fields on nerve fibers: Determination of excitation thresholds”. In: *IEEE Transactions on Biomedical Engineering* 39.12 (1992), pp. 1244–1254. ISSN: 00189294. DOI: `10.1109/10.184700`.

[96] I. Lerman, R. Hauger, L. Sorkin, J. Proudfoot, B. Davis, A. Huang, K. Lam, B. Simon, and D. G. Baker. “Noninvasive Transcutaneous Vagus Nerve Stimulation Decreases Whole Blood Culture-Derived Cytokines and Chemokines: A Randomized, Blinded, Healthy Control Pilot Trial”. In: *Neuromodulation* 19.3 (Apr. 2016), pp. 283–291. ISSN: 15251403. DOI: `10.1111/ner.12398`.

[97] H. Xiong, B. Qiu, and J. Liu. “An improved multi-swarm particle swarm optimizer for optimizing the electric field distribution of multichannel transcranial magnetic stimulation”. In: *Artificial Intelligence in Medicine* 104 (Apr. 2020), p. 101790. ISSN: 09333657. DOI: `10.1016/j.artmed.2020.101790`.

[98] Y. Chen, J. Wang, X. Wei, B. Deng, and Y. Che. “Particle swarm optimization of periodic deep brain stimulation waveforms”. In: *Proceedings of the 30th Chinese Control Conference*. IEEE. 2011, pp. 754–757.

[99] C. Martinelli, A. Coraddu, and A. Cammarano. “Experimental Parameter Identification of Nonlinear Mechanical Systems via Meta-heuristic Optimisation Methods”. In: 2024, pp. 215–223. DOI: `10.1007/978-3-031-36999-5{\_}28`.

[100] D. E. Goldberg. *Genetic Algorithms in Search, Optimization and Machine Learning*. 1st. USA: Addison-Wesley Longman Publishing Co., Inc., 1989. ISBN: 0201157675.

[101] D. Wang, D. Tan, and L. Liu. “Particle swarm optimization algorithm: an overview”. In: *Soft Computing* 22.2 (Jan. 2018), pp. 387–408. ISSN: 1432-7643. DOI: `10.1007/s00500-016-2474-6`.

[102] E. Peña, S. Zhang, S. Deyo, Y. Xiao, and M. D. Johnson. “Particle swarm optimization for programming deep brain stimulation arrays”. In: *Journal of Neural Engineering* 14.1 (Feb. 2017), p. 016014. ISSN: 1741-2560. DOI: `10.1088/1741-2552/aa52d1`.

[103] D. H. P. C. C. (DHPC). *DelftBlue Supercomputer (Phase 2)*. `https://www.tudelft.nl/dhpc/ark:/44463/DelftBluePhase2`. 2024.

A

ADDITIONAL FIGURES

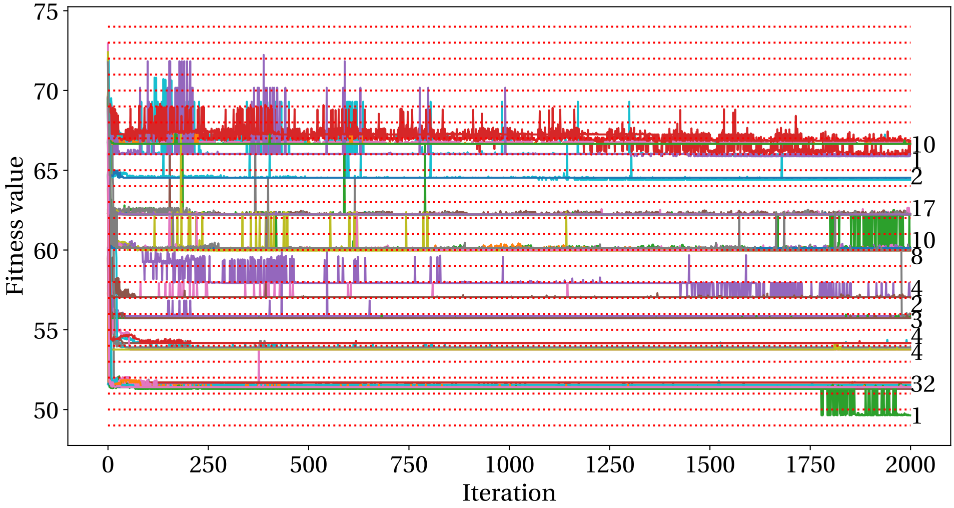

Figure A.1.: Fitness values unfiltered of the 98 runs over 2000 iterations

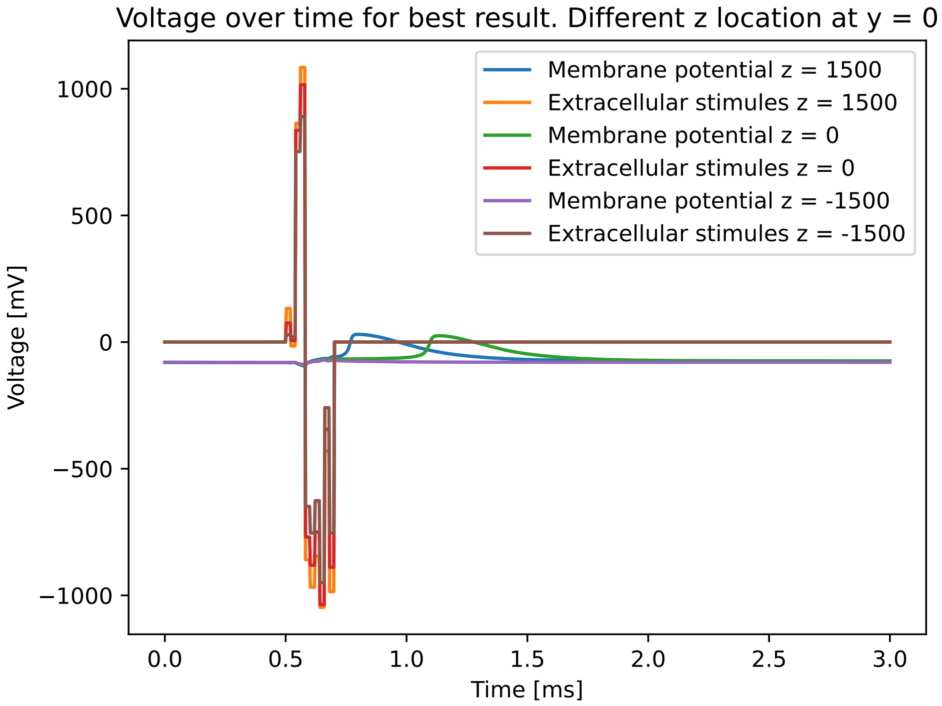

Figure A.2.: Extracellular potential of the axon at different locations during stimulation.

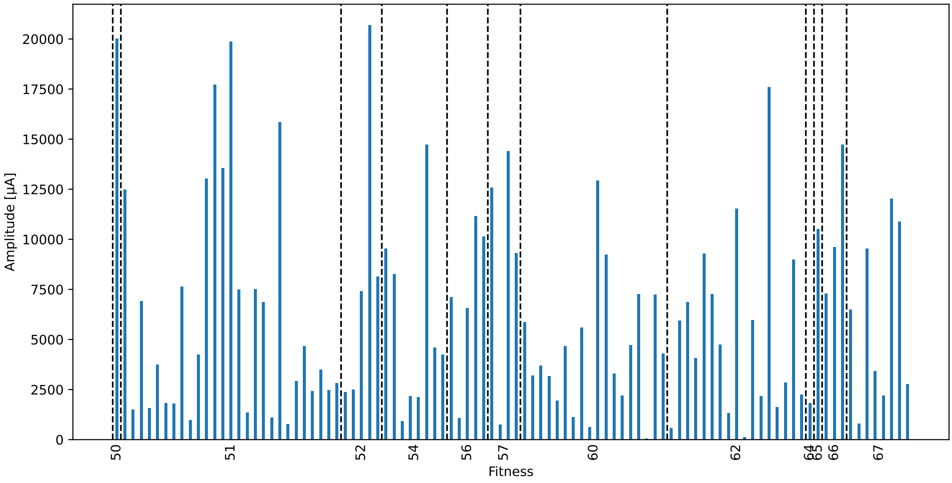

Figure A.3.: Symmetry over the y-axis.

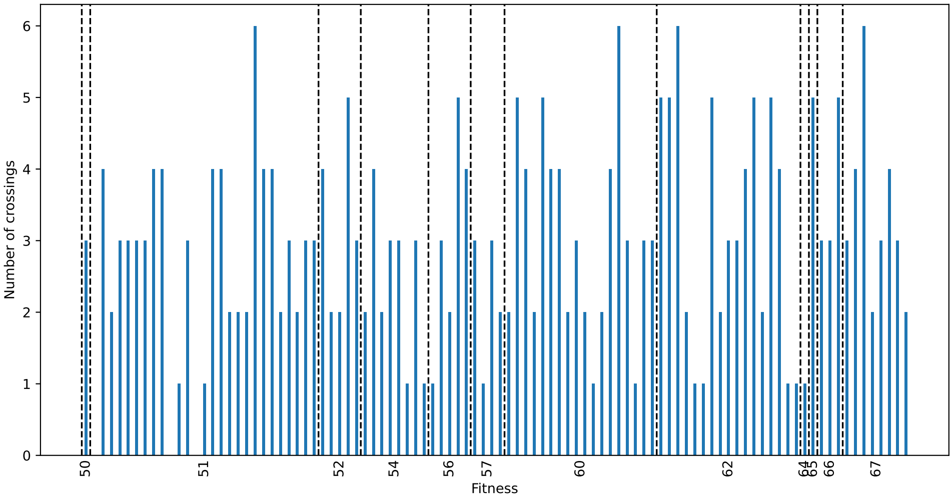

Figure A.4.: Number of signal crossings.

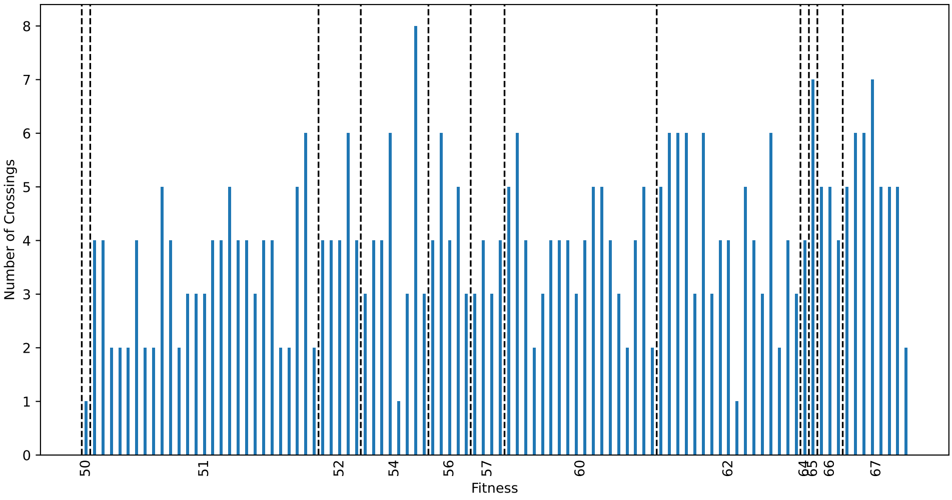

Figure A.5.: Number of zero crossings.